NTNU – Trondheim
Norwegian University of
Science and Technology

Constrained Hydrogel swelling in Biological Sensors

A Finite Element Method Approach

Hrafn Mar Sveinsson

Master of Science in Physics and Mathematics
Submission date: June 2012
Supervisor: Bjørn Torger Stokke, IFY
Co-supervisor: Professor Bjørn Helge Skallerud, Konstruksjonsteknikk
Associate Prof. Victorie Emile Prot, Konstruksjonsteknikk

Norwegian University of Science and Technology
Department of Physics

Constrained Hydrogel swelling in Biological Sensors: A Finite Element Method Approach

Sveinsson, Hrafn Mar

June 29, 2012

Abstract

Material models has been developed for anionic and/or cationic hydrogels, with a simulation framework implemented in *MATLAB* and the finite element software *ABAQUS*. The geometry of the simulations is a hemispheroidal hydrogel, divided into a core with a shell, covalently attached to an optical fiber. The material models have been used to estimate the chemical parameters of poly-acrylamide hydrogels containing anionic or cationic monomer groups. Simulations comparing free and constrained swelling has been conducted in order to determine the effect of the geometrical constriction to the optical fiber. Constrained hydrogel swelling featuring shells with different properties than the core was also investigated.

The aim of the study was to validate the material models and examine the effects of geometrical constrictions together with shell-impregnation. The anionic material model was shown to reproduce experimental swelling data, while the cationic material model only reproduced the data for ionic strength greater than 100 mM. Restricting the hydrogel to an optical fiber resulted in decreased change in volume and an increase in the axial swelling. The model was able to reproduce reported reduction in the swelling for an impregnated anionic hydrogel by using a neutral shell in the simulations, but failed to recreate the shape of the swelling curve. With the reduction of swelling as a basis, a new method for estimating thin-layer properties has been developed.

Sammendrag

Materialmodeller har blitt utviklet for anioniske og/eller kationiske hydrogeler, med et simuleringsrammeverk implementert i *MATLAB* og finite element simuleringspakken *ABAQUS*. Geometrien brukt i simuleringene er en halvkule av hydrogel, delt inn i en kjerne med et skall, kjemisk fastbundet til en optisk fiber. Materialmodellene har blitt brukt til å estimere de kjemiske parametrene til poly-acrylamide hydrogeler som inneholder enten anioniske eller kationiske monomergrupper. Simuleringer som sammenligner fri og geometrisk begrenset svelling har blitt gjennomført for å fastslå effekten av fastlimingen. Geometrisk begrenset hydrogelsvelling der det ble tatt hensyn til et nøytralt skall ble også undersøkt.

Målet med studien var å validere materialmodellene og undersøke effekten av geometriske begrensninger og impregnering av hydrogeler. Den anioniske materialmodellen viste seg å reprodusere eksperimentelle svelledata, mens den kationiske materialmodellen kun reproduserte dara for ionestyrke større enn 100 mM. Fastlimingen av en hydrogel til en optisk fiber viste seg å redusere volumendringene mens den aksielle svellingen økte. Modellen reproduserte rapportert reduksjon i svelling for en impregnert anionisk hydrogel ved å simulere et nøytralt skall utenpå kjernen, men kunne ikke gjenskape formen på svellekurven. Med utgangspunkt i svellereduksjonen er det blitt utviklet en ny metode for Ã¥ estimere egenskapene til tynne lag.

Preface

This masters thesis expands on experiences from a preliminary project work, where it was shown that constraining an anionic hydrogel affects the swelling significantly. The aim of this work was to complete the material model with a cationic module and to develop a framework for handling hydrogels impregnated with a layer, and thus being able to study the effects of anionic hydrogels with a non-anionic shell.

I would like to thank all who has contributed to this work. My supervisor Bjørn T. Stokke, who has never failed to give me useful insights. You have been an invaluable support during the entire process. My second supervisor Victorien E. Prot, for helping me to solve one challenging problem after another. You made me able to achieve my goals. My third supervisor Bjørn Skallerud, without whom this interdisciplinary study would not have been initiated. I would also like to thank Kamila Gawel and Ming Gao for their contribution and materials provided.

A warm and special thanks goes to my friends and family for the support, and to my fiancé Sonja Kistenich in particular, for keeping my head up and my eyes straight.

Contents

1 Introduction

A hydrogel is a network of covalently cross-linked polymer chains that absorbs the solvent molecules it is being immersed in. Since the swelling can be affected by external factors like pH, ion strength and the concentration of certain molecules, the application of hydrogels are numerous. In [1] it has been suggested to use hydrogels as microvalves able to open and close depending on the chemical conditions in the solution. A hydrogel transducer system has been developed at Norwegian University of Science and Technology, based on an interferometric readout platform developed by Invivosense[2][3]. The transducer system has a capability of measuring hydrogel swelling with nanometer resolution.

There are systematical differences in the chemically predicted and the experimentally evident defining parameters of the polymerized hydrogels [4][5]. The gel parameters will thus have to estimated by the means of mathematical models. Further challenges with parameter estimation arises when impregnating a hydrogel with a thin layer with different properties. The basis of a chemical estimate can be even more restricted. The defining parameters of the coating can be measured using several methods[6], or it can be estimated by fitting experimental swelling data with simulation results.

The swelling behavior changes when the hydrogel is under geometrical constrictions, and the swelling can only be solved analytically for a few special cases. By using finite element simulations, estimates can still be done for arbitrary geometries and constrictions[1][7]. In the transducer setup in [2][3][8], the hydrogel is covalently attached to an optical fiber and thus restricted along that interface.

In the present study, a material model for cationic hydrogels has been developed and used together with the anionic material model in [1]. A simulation setup for the geometry in [2][3][8] has been implemented in combination with the material models. The simulation model supports the division of the hydrogel into a core and a shell with a different set of parameters. The simulation has been validated for both material models, and the effects of hydrogel impregnation was investigated. The latter was used to develop a method for estimating the crosslink density of an impregnation layer, by generating contour plots relating the crosslink density and the thickness of the layer and comparing an equicontour with experimental data.

2 Theory

2.1 Continuum mechanics

The mathematics of this section is based on [9], while the symbols referred to are listed in table 1. The deformation gradient is defined as the change in true coordinates related to the reference system:

$$\mathbf{F} = \frac{\partial \mathbf{x}}{\partial \mathbf{X}}. \tag{2.1.1}$$

Figure 1 shows the transition from the initial dry state, through the swollen, stress free state to the swollen, deformed state of the hydrogel. The propagation from a state to another can be represented by multiplication with the deformation gradient of the transition:

$$\mathbf{K}_d \rightarrow \mathbf{K}_0 : \mathrm{d}\mathbf{r}_0 = \mathbf{F}_0 \, \mathrm{d}\mathbf{r}_d \tag{2.1.2}$$

$$\mathbf{K}_0 \rightarrow \mathbf{K} : \mathrm{d}\mathbf{r} = \mathbf{F} \, \mathrm{d}\mathbf{r}_0. \tag{2.1.3}$$

$$\mathbf{K}_d \rightarrow \mathbf{K} : \mathrm{d}\mathbf{r} = \mathbf{F}_{tot} \, \mathrm{d}\mathbf{r}_d. \tag{2.1.4}$$

Table 1: Parameter definitions of section 2.1. For specific indices, see figure 1.

$\mathbf{X}$	Lagrangian coordinates; Reference coordinates
$\mathbf{x}$	Eulerian coordinates; Field of deformation
$\mathbf{r}$	Position vector
$\mathrm{d}\mathbf{r}$	Line element
$\mathbf{F}$	Deformation gradient
$\mathbf{C}$	Greens deformation tensor. Right deformation tensor
$\mathbf{B}$	Left deformation tensor
I_1	First principal invariant of $\mathbf{C}$
$\bar{I}_1$	Modified first principal invariant of $\mathbf{C}$
J	Jacobian. Third principal invariant of $\mathbf{F}$
λ_i	Principal stretch for the ortogonal directions 1, 2 and 3
λ_0	Uniform principal stretch for the reference state.
$\mathbf{s}$	Tensor of nominal stress
$\boldsymbol{\sigma}$	Stress tensor

Combining (2.1.2) with (2.1.3) gives the expression

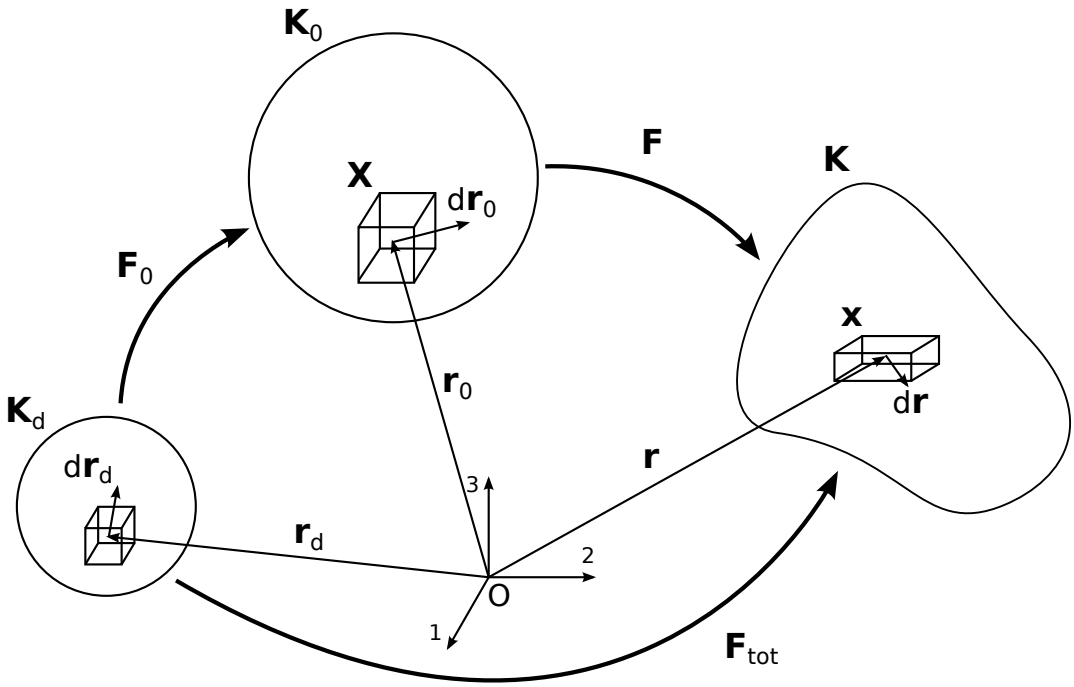

Figure 1: State diagram showing how the line elements and deformation gradients are related to the different states $\mathbf{K}$, where the indices d and 0 indicate dry state and reference state respectively. For the current state there is no index. The total deformation gradient $\mathbf{F}_{tot}$ is decomposed into a component $\mathbf{F}_0$, making the system undergo homogeneous swelling, and a component $\mathbf{F}$ deforming the reference state to the current state.

$$\mathbf{K}_d \to \mathbf{K}_0 \to \mathbf{K} : \mathrm{d}\mathbf{r} = \mathbf{F}\mathbf{F}_0 \, \mathrm{d}\mathbf{r}_d, \tag{2.1.5}$$

which is equivalent to (2.1.4). This yields a relation between the deformation gradients,

$$\mathbf{F}_{tot} = \mathbf{F}_0\mathbf{F}, \tag{2.1.6}$$

showing that the deformation gradients can be combined by multiplication in order to represent the transition through several states. The left and right deformation tensors are given by

$$\mathbf{B} = \mathbf{F}\mathbf{F}^{\mathrm{T}} \tag{2.1.7}$$

and

$$\mathbf{C} = \mathbf{F}^{\mathrm{T}}\mathbf{F}. \tag{2.1.8}$$

respectively. Two principal invariants of the deformation gradient are

$$I_1 = \mathrm{tr}\,(\mathbf{B}) = \mathrm{tr}\,(\mathbf{C}) = \lambda_1^2 + \lambda_2^2 + \lambda_3^2 \tag{2.1.9}$$

and

$$J = \det \mathbf{F} = \lambda_1 \lambda_2 \lambda_3. \tag{2.1.10}$$

They are both scalar with unit 1 and independent of the choice of reference coordinates. The Jacobian of the reference state is given by

$$J_0 = \det \mathbf{F}_0 = \lambda_0^3. \tag{2.1.11}$$

The Jacobians represent the change in volume due to a transition. The Jacobian for the total transition $\mathbf{K}_d \rightarrow \mathbf{K}$ can be found through the determinant of (2.1.6),

$$\det \mathbf{F}_{tot} = \det \mathbf{F}_0 \cdot \det \mathbf{F}, \tag{2.1.12}$$

and inserting (2.1.10-2.1.11):

$$\det \mathbf{F}_{tot} = J_0 J. \tag{2.1.13}$$

The right deformation tensor for the same transition is given by

$$\mathbf{C}_{tot} = \mathbf{F}_{tot}^{\mathrm{T}} \mathbf{F}_{tot}. \tag{2.1.14}$$

Inserting (2.1.6) and (2.1.8) into (2.1.14) yields

$$\mathbf{C}_{tot} = \mathbf{F}_0^{\mathrm{T}} \mathbf{C} \mathbf{F}_0 = \lambda_0 \mathbf{1}^{\mathrm{T}} \mathbf{C} \lambda_0 \mathbf{1} = {\lambda_0}^2 \mathbf{C}, \tag{2.1.15}$$

since $\mathbf{F}_0$ describes a state of homogeneous swelling and thus is a diagonal matrix with all its eigenvalues equal to λ_0. This leads to an expression of the total first invariant of the system given by

$$I_{1,tot} = \mathrm{tr}({\lambda_0}^2 \mathbf{C}) = {\lambda_0}^2 I_1 = \lambda_0^2(\lambda_1^2 + \lambda_2^2 + \lambda_3^2). \tag{2.1.16}$$

The second Piola-Kirchhoff stress tensor is defined as

$$\mathbf{S} \equiv 2\frac{\partial U}{\partial \mathbf{C}} = 2\frac{\partial U}{\partial I_1}\mathbf{1} + 2\frac{\partial U}{\partial J}\frac{\partial J}{\partial \mathbf{C}}, \tag{2.1.17}$$

where U is the free energy density function, to be investigated in the next section. The following relation holds:

$$\frac{\partial J}{\partial \mathbf{C}} = \frac{1}{2} J \mathbf{C}^{-1}. \tag{2.1.18}$$

The Cauchy stress tensor is defined as

$$\boldsymbol{\sigma} \equiv \frac{1}{J}\mathbf{F}\mathbf{s}\mathbf{F}^{\mathrm{T}}. \tag{2.1.19}$$

When inserting (2.1.17-2.1.18) into (2.1.19), and recognizing (2.1.7), $\boldsymbol{\sigma}$ can be expressed as

$$\boldsymbol{\sigma} = \frac{2}{J}\frac{\partial U}{\partial I_1}\mathbf{B} + \frac{\partial U}{\partial J}\mathbf{1}. \tag{2.1.20}$$

I_1 can also be expressed by the modified first invariant:

$$I_1 = J^{2/3}\bar{I}_1. \tag{2.1.21}$$

Combining (2.1.16) and (2.1.21) yields:

$$I_{1,tot} = {\lambda_0}^2 I_1 = (J_0 J)^{2/3}\bar{I}_1. \tag{2.1.22}$$

2.2 Polymer network elasticity

The behavior of a swollen polymer network and the different free energy density functions arising from the different swelling phenomena will be outlined in this section. The parameters used are given in tables 2 and 3. It is first necessary to establish some relations regarding the chemical potential of the free species in figure 2 and the different ways to express their concentrations. The chemical potential for the different mobile species, indicated by the subscript, is given by [1][10]:

$$\mu_+ = k_B T \ln\left(\frac{\bar{c}_+}{c_+^{ref}}\right) \tag{2.2.1}$$

$$\mu_- = k_B T \ln\left(\frac{\bar{c}_-}{c_-^{ref}}\right) \tag{2.2.2}$$

$$\mu_{H^+} = k_B T \ln\left(\frac{\bar{c}_{H^+}}{c_{H^+}^{ref}}\right). \tag{2.2.3}$$

The chemical potential for the solvent is given by:

$$\mu_S = -k_B T v_S \sum_{\alpha \neq S} \bar{c}_\alpha. \tag{2.2.4}$$

The relation between the nominal and true concentration is

$$C_\alpha = c_\alpha \det \mathbf{F}_{tot}, \tag{2.2.5}$$

while the relation between the volumetric and molar concentration is

$$c_\alpha = N_A[\alpha]. \tag{2.2.6}$$

The condition of molecular incompressibility can be written as

$$1 + v_S C_S = \det \mathbf{F}_{tot} = J_0 J \tag{2.2.7}$$

where 1 represents the dry network and $v_S C_S$ the solvent. For $v_S C_S \gg 1$ (2.2.7) reduces to

$$v_S C_S \simeq J_0 J. \tag{2.2.8}$$

In an anionic polymer network the following reaction takes place

$$AH \rightleftharpoons A^- + H^+ \tag{2.2.9}$$

yielding negatively charged monomer groups upon dissociation. This can be expressed in terms of the acid dissociation constant, K_a:

$$K_a^{an} = \frac{[H^+][A^-]}{[AH]}. \tag{2.2.10}$$

The total number of ionizable monomer groups is conserved through the relation

$$C_{AH}(\mathbf{X}) + C_{A^-}(\mathbf{X}) = \frac{f}{v}. \tag{2.2.11}$$

For a cationic polymer network the following reaction takes place

$$A + H_2O \rightleftharpoons AH^+ + OH^- \tag{2.2.12}$$

and it can be rewritten as

Table 2: Various parameters described in terms of species, α, shown in figure 2. .

$[\alpha]$	Molar concentration
C_α	Nominal volumetric concentration inside the network
c_α	True concentration inside the network
$\bar{c}_\alpha$	Concentration in the external solution
c_α^{ref}	Reference concentration
n_α	Number of species in the polymer network
$\bar{n}_\alpha$	Number of species in the external solution
μ_α	Chemical potential of species

Table 3: Various parameters used in section 2.2.

k_B	J K^{-1}	Boltzmann constant
N_A	mol^{-1}	Avogadro's number
T	K	Temperature
f	1	Fraction of monomers with ionizable group
v	m^3	Volume per monomer
v_S	m^3	Volume per solvent molecule
V_0	m^3	Polymer network volume
ΔS	J K^{-1}	Entropy
ΔH	J	Enthalpy
ΔF	J	Free energy
U	J m^{-3}	Free energy density function
N	m^{-3}	Network crosslink density
χ	1	Flory-Huggins parameter
ϕ_N	1	Polymer volume fraction
ϕ_S	1	Solvent volume fraction
$\gamma_{\alpha,\delta}$	J M^{-1}	Molar heat of association/dissociation

$$AH^+ \rightleftharpoons A + H^+, \tag{2.2.13}$$

yielding positively charged monomer groups upon association. Expressed through K_a (2.2.13) takes the form

$$K_a^{cat} = \frac{[H^+][A]}{[AH^+]}. \tag{2.2.14}$$

The conservation of ionizable groups in the cationic network will be

$$C_A(\mathbf{X}) + C_{AH^+}(\mathbf{X}) = \frac{f}{v}. \tag{2.2.15}$$

The free energy of the system is given by

$$\Delta F = \Delta H - T\Delta S. \tag{2.2.16}$$

The free energy density function, or strain energy density function, is given by

$$U = \frac{\Delta F}{V_0}. \tag{2.2.17}$$

2.2.1 Stretching of the network

When the network swells, the total contribution to the entropy due to stretching the monomer chains, is given by [11]:

$$\Delta S_{str} = -\frac{1}{2} N k_B [l_1^2 + l_2^2 + l_3^2 - 3 - 2\ln(l_1 l_2 l_3)] \tag{2.2.18}$$

where the entropy is relative to the unswollen, or dry, network with unit volume. With $l_i = \lambda_0 \lambda_i$, this becomes

$$\Delta S_{str} = -\frac{1}{2} N k_B [\lambda_0^2(\lambda_1^2 + \lambda_2^2 + \lambda_3^2) - 3 - 2\ln(\lambda_0^3 \lambda_1 \lambda_2 \lambda_3)]. \tag{2.2.19}$$

Recalling the relations (2.1.13) and (2.1.9) this can be expressed as

$$\begin{aligned} \Delta S_{str} &= -\frac{1}{2} N k_B [\lambda_0^2 I_1 - 3 - 2\ln(J_0 J)] \\ &= -\frac{1}{2} N k_B J_0 [\frac{1}{\lambda_0} I_1 - \frac{3}{J_0} - \frac{2}{J_0}\ln(J_0 J)]. \end{aligned} \tag{2.2.20}$$

Insertion of (2.2.20) and (2.2.16) with $\Delta H = 0$ and $V_0 = 1$ into (2.2.17) thus gives the free energy of stretching per volume:

$$U_{str} = \frac{1}{2} N k_B T J_0 [\frac{1}{\lambda_0} I_1 - \frac{3}{J_0} - \frac{2}{J_0}\ln(J_0 J)]. \tag{2.2.21}$$

2.2.2 Mixing of polymers and solvent

The entropy of mixing between two species is given by:

$$\Delta S_{mix} = -k_B [n_1 \ln \phi_1 + n_2 \ln \phi_2]. \tag{2.2.22}$$

The entropy of mixing of an assembly of free monomers with solvent molecules is shown[11] to satisfy (2.2.22):

$$\Delta S_M = -k_B [n_S \ln \phi_S + N \ln \phi_N]. \tag{2.2.23}$$

The enthalpy of mixing for network and solvent is given by [12] as

$$\Delta H_M = k_B T n_S \phi_N \chi. \tag{2.2.24}$$

If $\chi > 0$, same-same interactions between the molecules is preferred and heat is required to mix, while heat is released by mixing if $\chi < 0$. Inserting

(2.2.23) and (2.2.24) into (2.2.16) yields the free energy of mixing of network and solvent:

$$\Delta F_M = k_B T[n_S \ln(1-\phi_N) + N \ln \phi_N + n_S \phi_N \chi] \tag{2.2.25}$$

For a swollen network, $n_S \gg N$. It then follows that

$$\Delta F_M = k_B T n_S[\ln(1-\phi_N) + \phi_N \chi] \tag{2.2.26}$$

and

$$n_S = V_0 C_S. \tag{2.2.27}$$

The volume fraction of the network can be found through the condition of molecular incompressibility (2.2.7):

$$\phi_N = \frac{1}{1+v_S C_S} = \frac{1}{J_0 J} \tag{2.2.28}$$

Inserting (2.2.26) together with (2.2.27) and (2.2.28) into (2.2.17) gives the free energy density of mixing of network and solvent:

$$U_{mix} = \frac{k_B T}{v_s}\left[(1-J_0 J)\ln(1-\frac{1}{J_0 J}) + \chi\left(1-\frac{1}{J_0 J}\right)\right]. \tag{2.2.29}$$

2.2.3 Mixing of the free ions

Free energy of mixing for the mobile ions is given by [13]:

$$U_{ion} = k_B T \sum_{\alpha \neq S} C_\alpha \left(\ln \frac{C_\alpha}{v_S C_S c_\alpha^{ref}} - 1\right) \tag{2.2.30}$$

Inserting (2.2.5) and the approximation (2.2.8) into (2.2.30) gives the following expression for the free energy of mixing for the mobile ions:

$$U_{ion} = k_B T J_0 J \sum_{\alpha \neq S} c_\alpha \left(\ln \frac{c_\alpha}{c_\alpha^{ref}} - 1\right). \tag{2.2.31}$$

2.2.4 Dissociation and association equilibria

The change in entropy for the distribution of associated, α, and dissociated, δ, ionizable groups is according to (2.2.22):

$$\Delta S_{acid} = -k_B V_0 \cdot J_0 J \left[c_\alpha \ln\left(\frac{c_\alpha}{c_\alpha + c_\delta}\right) + c_\delta \ln\left(\frac{c_\delta}{c_\alpha + c_\delta}\right)\right] \tag{2.2.32}$$

and the enthalpy of association and dissociation is:

$$\Delta H_{\alpha,\delta} = J_0 J \cdot \gamma_{\alpha,\delta} c_{\alpha,\delta} \tag{2.2.33}$$

$$U_{\alpha,\delta} = -T\Delta S_{acid} + \Delta H_{\alpha,\delta} \tag{2.2.34}$$

Using (2.2.5), (2.2.35) and (2.2.36) can be expressed as

$$c_{AH} + c_{A^-} = \frac{f}{v J_0 J} \tag{2.2.35}$$

$$c_A + c_{AH^+} = \frac{f}{v J_0 J}. \tag{2.2.36}$$

For anionic dissociation and cationic association, (2.2.34) can be expressed as

$$U_{dis} = k_B T \cdot J_0 J \left[c_{AH} \ln\left(\frac{c_{AH}}{c_{A^-} + c_{AH}}\right) + c_{A^-} \ln\left(\frac{c_{A^-}}{c_{A^-} + c_{AH}}\right)\right] + J_0 J \cdot \gamma_{dis} c_{A^-} \tag{2.2.37}$$

and

$$U_{as} = k_B T \cdot J_0 J \left[c_{AH^+} \ln\left(\frac{c_{AH^+}}{c_{AH^+} + c_A}\right) + c_A \ln\left(\frac{c_A}{c_{AH^+} + c_A}\right)\right] + J_0 J \cdot \gamma_{ass} c_{AH^+} \tag{2.2.38}$$

respectively.

2.3 Inhomogeneous swelling

The mechanical work done by the forces of deformation is dependent on the body force, B_i, and the traction force, T_i, along the surface of the hydrogel:

$$W_{mech} = \int B_i \delta x_i \, \mathrm{d}V + \int T_i \delta x_i \, \mathrm{d}S. \tag{2.3.1}$$

Even for inhomogeneous swelling it is assumed that volumes on a microscopic level swell homogeneously. The total contribution to Helmholtz free energy, A, of the gel is thus given by:

$$A_{gel} = \int U \, \mathrm{d}V, \tag{2.3.2}$$

where U denotes the free energy density function. The change in free energy in the external solution is given by

$$\delta A_{sol} = \mu_S \delta \bar{n}_S + \mu_{H^+} \delta \bar{n}_{H^+} + \mu_+ \delta \bar{n}_+ + \mu_- \delta \bar{n}_-. \tag{2.3.3}$$

The equilibrium conditions are found when the total variation of Helmholtz free energy of the system is zero:

$$\begin{aligned} \delta A &= \delta A_{gel} + \delta A_{sol} - W_{mech} \\ &= \int \delta U \, \mathrm{d}V + \mu_S \delta \bar{n}_S + \mu_{H^+} \delta \bar{n}_{H^+} + \mu_+ \delta \bar{n}_+ + \mu_- \delta \bar{n}_- \\ &\quad - \int B_i \delta x_i \, \mathrm{d}V - \int T_i \delta x_i \, \mathrm{d}S = 0. \end{aligned} \tag{2.3.4}$$

The negative ions, positive ions and solvent molecules don't react chemically with the polymer network, and the total number of free species is thus conserved. The balance of each species across the surface of the network can be expressed as

$$\int \delta C_-(\mathbf{X}) \, \mathrm{d}V = -\delta \bar{n}_- \tag{2.3.5}$$

$$\int \delta C_+(\mathbf{X}) \, \mathrm{d}V = -\delta \bar{n}_+ \tag{2.3.6}$$

$$\int \delta C_S(\mathbf{X}) \, \mathrm{d}V = -\delta \bar{n}_S. \tag{2.3.7}$$

The condition of electroneutrality must be fulfilled both inside and outside the network. In the external solution, the condition can be expressed in terms of the number of each mobile species:

$$\bar{n}_{H^+} + \bar{n}_+ = \bar{n}_-. \tag{2.3.8}$$

To express this condition inside the network, together with the conservation of H^+, the fixed charges and the properties of the ionizable monomers in the gel must also be taken into account. The condition of electroneutrality inside an anionic network can be expressed in terms of the concentration of the different charged species present:

$$C_{H^+}(\mathbf{X}) + C_+(\mathbf{X}) = C_{A^-}(\mathbf{X}) + C_-(\mathbf{X}). \tag{2.3.9}$$

The conservation of H^+ within the anionic network and across its surface can be expressed as

$$\int \delta C_{H^+}(\mathbf{X})\ \mathrm{d}V - \int \delta C_{A^-}(\mathbf{X})\ \mathrm{d}V = -\delta \bar{n}_{H^+}. \tag{2.3.10}$$

Inserting (2.3.9) into (2.3.10) gives the following expression for the change in protons in the external solution:

$$\delta \bar{n}_{H^+} = \int \delta C_+(\mathbf{X})\ \mathrm{d}V - \int \delta C_-(\mathbf{X})\ \mathrm{d}V = \delta \bar{n}_+ - \delta \bar{n}_- \tag{2.3.11}$$

where the last step can be recognized in (2.3.5-2.3.6). (2.3.11) is in accordance with (2.3.8) and makes it possible to express (2.3.3) as

$$\delta A_{sol} = \mu_S \delta \bar{n}_S + (\mu_+ - \mu_{H^+})\delta \bar{n}_+ + (\mu_- + \mu_{H^+})\delta \bar{n}_-. \tag{2.3.12}$$

The condition of electroneutrality will for the cationic network take the form

$$C_{H^+}(\mathbf{X}) + C_+(\mathbf{X}) + C_{AH^+}(\mathbf{X}) = C_-(\mathbf{X}), \tag{2.3.13}$$

while the conservation of H^+ is expressed by

$$\int \delta C_{H^+}(\mathbf{X})\ \mathrm{d}V + \int \delta C_{AH^+}(\mathbf{X})\ \mathrm{d}V = -\delta \bar{n}_{H^+}. \tag{2.3.14}$$

Inserting (2.3.13) into (2.3.14) will also yield (2.3.11) and thus (2.3.12). The free energy density function can for both anionic and cationic gels be written as a function of all the independent parameters:

$$U = U(\mathbf{F}, C_+, C_-, C_{H^+}). \tag{2.3.15}$$

By applying the chain rule on (2.3.2) considering the variables in (2.3.15) and inserting it together with (2.3.12) into (2.3.4), a new expression for the conversion of the Helmholtz free energy at equilibrium is found:

$$
\begin{aligned}
\delta A = &\int \left[\frac{\partial S_{iK}}{\partial X_K} + B_i\right] \delta x_i \,\mathrm{d}V \\
&+ \int \left[s_{iK} N_K - T_i\right] \delta x_i \,\mathrm{d}S \\
&+ \int \left[\tfrac{\partial U}{\partial C_+} - (\mu_+ - \mu_{H^+})\right] \delta C_+ \,\mathrm{d}V \\
&+ \int \left[\tfrac{\partial U}{\partial C_-} - (\mu_- + \mu_{H^+})\right] \delta C_- \,\mathrm{d}V \\
&+ \int \tfrac{\partial U}{\partial C_{H^+}} \delta C_{H^+} \,\mathrm{d}V = 0
\end{aligned}
\tag{2.3.16}
$$

where N_K is the normal vector and the index form of the tensor of nominal stress, s_{iK}, is given as

$$
s_{iK} = \frac{\partial U}{\partial F_{iK}} - \frac{\mu_S}{v_S} (F_{iK}^{-1})^{\mathrm{T}} J_0 J. \tag{2.3.17}
$$

F_{iK} is the index form of the deformation gradient. For (2.3.16) to hold, each of its integral terms must also be equilibrated, and a couple of relations can thus be identified. For the interior and the surface of the network,

$$
-\frac{\partial s_{iK}}{\partial X_K} = B_i \tag{2.3.18}
$$

and

$$
s_{iK} N_K = T_i \tag{2.3.19}
$$

must hold respectively. The conditions for ionic equilibrium can be identified as

$$
\frac{\partial U(\mathbf{F}, C_+, C_-, C_{H^+})}{\partial C_+} = \mu_+ - \mu_{H^+} \tag{2.3.20}
$$

$$
\frac{\partial U(\mathbf{F}, C_+, C_-, C_{H^+})}{\partial C_-} = \mu_- + \mu_{H^+}, \tag{2.3.21}
$$

while the protonic equilibrium is given as

$$
\frac{\partial U(\mathbf{F}, C_+, C_-, C_{H^+})}{\partial C_{H^+}} = 0. \tag{2.3.22}
$$

2.4 Specific material model

The free energy density function of the gel is is assumed [12][1] to be the a sum of different contributions. The network poroelastic contribution, U_1, is the sum of the free energy density of deformation and mixing of the entire network

$$U_1 = U_{str} + U_{mix} \tag{2.4.1}$$

while the ionizable contribution, U_2, is the sum of the free energy density of electrostatic and dissociation/association contributions of the ionizable monomer groups:

$$U_2 = U_{ion} + U_{dis,as}. \tag{2.4.2}$$

The free energy density function of the system is thus

$$U = U_1 + U_2. \tag{2.4.3}$$

Recalling (2.2.21) gives the contribution from stretching of the network:

$$U_{str} = k_B T \cdot J_0 \frac{N}{2} [\frac{1}{\lambda_0} I_1 - \frac{3}{J_0} - \frac{2}{J_0} \ln(J_0 J)]. \tag{2.4.4}$$

Setting $v_s = v$ in (2.2.29) gives the contribution from mixing of the network:

$$U_{mix} = \frac{k_B T \cdot J_0}{v} \left[(\frac{1}{J_0} - J) \ln(1 - \frac{1}{J_0 J}) + \chi \left(1 - \frac{1}{J_0^2 J} \right) \right]. \tag{2.4.5}$$

Inserting for α in (2.2.31) gives the electrostatic contribution from the ionizable groups:

$$\begin{aligned} U_{ion} = k_B T \cdot J_0 J \Bigg[& c_{H^+} \ln \frac{c_{H^+}}{c_{H^+}^{ref}} + c_+ \ln \frac{c_+}{c_+^{ref}} \\ & + c_- \ln \frac{c_-}{c_-^{ref}} - (c_{H^+} + c_+ + c_-) \Bigg]. \end{aligned} \tag{2.4.6}$$

For anionic dissociation and cationic association, (2.2.37-2.2.38) can be expressed as

$$U_{dis} = k_B T \cdot J_0 J \left\{ \left[c_{AH} \ln \left(\frac{c_{AH}}{c_{A^-} + c_{AH}} \right) + c_{A^-} \ln \left(\frac{c_{A^-}}{c_{A^-} + c_{AH}} \right) \right] + \frac{1}{k_B T} \gamma_{dis} c_{A^-} \right\} \tag{2.4.7}$$

and

$$U_{as} = k_B T \cdot J_0 J \left\{ \left[c_{AH^+} \ln \left(\frac{c_{AH^+}}{c_{AH^+} + c_A} \right) + c_A \ln \left(\frac{c_A}{c_{AH^+} + c_A} \right) \right] + \frac{1}{k_B T} \gamma_{as} c_{AH^+} \right\} \tag{2.4.8}$$

respectively. Combining (2.4.4) and (2.4.5) yields

$$U_1 = U_{str} + U_{mix} = \frac{k_B T}{v/J_0} \left\{ \frac{1}{2} N v \left[\frac{1}{\lambda_0} I_1 - \frac{3}{J_0} - \frac{2}{J_0} \log(J_0 J) \right] - \left[(J - \frac{1}{J_0}) \log(\frac{J}{J - \frac{1}{J_0}}) + \frac{\chi}{J_0^2 J} \right] \right\}. \tag{2.4.9}$$

For both anionic and cationic networks, differentiation of U with respect to C_+ and C_- and recalling (2.2.5) yields

$$\frac{\delta U}{\delta C_+} = k_B T \left[\ln \left(\frac{c_+}{c_+^{ref}} \right) - \ln \left(\frac{c_{H^+}}{c_{H^+}^{ref}} \right) \right] \tag{2.4.10}$$

$$\frac{\delta U}{\delta C_-} = k_B T \left[\ln \left(\frac{c_-}{c_-^{ref}} \right) + \ln \left(\frac{c_{H^+}}{c_{H^+}^{ref}} \right) \right] \tag{2.4.11}$$

when treating γ as an unknown constant. The value of γ can be found by solving (2.3.22) and will be shown below to differ between the two cases. (2.4.10 - 2.4.11) can be compared with (2.3.20 - 2.3.21) and (2.2.1 - 2.2.3) to give the Donnan equations,

$$c_+ = \bar{c}_+ \frac{c_{H^+}}{\bar{c}_{H^+}} \tag{2.4.12}$$

$$c_- = \bar{c}_- \frac{\bar{c}_{H^+}}{c_{H^+}}, \tag{2.4.13}$$

thus allowing the ion concentrations inside the network to be expressed explicitly by c_{H^+} and the known system parameters such as the external ion concentrations. Solutions for c_{H^+} must be evaluated separately for anionic and cationic networks.

2.4.1 Anionic dissociation

Using (2.2.5), (2.3.9) can be expressed as

$$c_{A^-} = c_{H^+} + c_+ - c_-, \tag{2.4.14}$$

allowing (2.2.35) to be rewritten:

$$c_{AH} = \frac{f}{vJ_0J} - (c_{H^+} + c_+ - c_-). \tag{2.4.15}$$

Solving (2.3.22) gives the following expression:

$$c_{H^+}^{ref} e^{-\frac{\gamma_{dis}}{k_B T}} = \frac{c_{H^+} c_{A^-}}{\frac{f}{vJ_0J} - c_{A^-}}. \tag{2.4.16}$$

By recalling (2.2.6), the right side of (2.4.16) can be identified as the right side of (2.2.10) multiplied by N_A. (2.4.16) can thus be expressed as

$$\frac{c_{H^+}(c_{H^+} + c_+ - c_-)}{\frac{f}{vJ_0J} - (c_{H^+} + c_+ - c_-)} = N_A K_a, \tag{2.4.17}$$

where

$$N_A K_a = c_{H^+}^{ref} e^{-\frac{\gamma_{dis}}{k_B T}}. \tag{2.4.18}$$

An implicit expression for vc_{H^+} can be found by inserting (2.4.12 -2.4.13) into (2.4.17):

$$\begin{aligned} &\left(1 + \frac{v\bar{c}_+}{v\bar{c}_{H^+}}\right)(vc_{H^+})^3 + \left(1 + \frac{v\bar{c}_+}{v\bar{c}_{H^+}}\right) vN_A K_a (vc_{H^+})^2 \\ &- \left[\frac{f}{J_0 J} vN_A K_a + v\bar{c}_{H^+} v\bar{c}_-\right](vc_{H^+}) - vN_A K_a v\bar{c}_{H^+} v\bar{c}_- = 0. \end{aligned} \tag{2.4.19}$$

This is a cubic equation with coefficients

$$a = 1 + \frac{v\bar{c}_+}{v\bar{c}_{H^+}} \tag{2.4.20}$$

$$b = a \cdot vN_AK_a \tag{2.4.21}$$

$$c = -\left[\frac{f}{J_0J}vN_AK_a + v\bar{c}_{H^+}v\bar{c}_-\right] \tag{2.4.22}$$

$$d = -vN_AK_a \cdot v\bar{c}_{H^+}\, v\bar{c}_- \tag{2.4.23}$$

and can be solved for vc_{H^+} by applying the solution of the cubic equation given in appendix A.1:

$$vc_{H^+} = \sqrt[3]{q + \sqrt{q^2 - p^3}} + \sqrt[3]{q - \sqrt{q^2 - p^3}} - \frac{b}{3a} \tag{2.4.24}$$

where

$$p = \frac{c}{3a} - \left(\frac{b}{3a}\right)^2 \tag{2.4.25}$$

$$q = \frac{1}{2}\left(\frac{bc}{3a^2} - \frac{d}{a}\right) - \left(\frac{b}{3a}\right)^3. \tag{2.4.26}$$

It should be kept in mind that the term $\sqrt{q^2 - p^3}$ in (2.4.24) can be complex. This will be discussed further in section 2.5. The non-poroelastic contribution of the anionic strain energy density function takes the form

$$U_2 = U_{ion} + U_{dis}. \tag{2.4.27}$$

The anionic material model has been both documented and implemented in [1] and will not be the focus of the present study. The non-poroelastic contribution to the cationic material model will on the other hand be presented below.

2.4.2 Cationic association

Using (2.2.5), (2.3.13) can be expressed as

$$c_{AH^+} = c_- - (c_{H^+} + c_+) \tag{2.4.28}$$

allowing (2.2.36) to be rewritten:

$$c_A = \frac{f}{vJ_0J} + (c_{H^+} + c_+ - c_-). \tag{2.4.29}$$

Solving (2.3.22) gives the following expression:

$$c_{H^+}^{ref} e^{\frac{\gamma_{as}}{k_B T}} = \frac{c_{H^+}(\frac{f}{vJ_0J} - c_{AH^+})}{c_{AH^+}}. \tag{2.4.30}$$

By recalling (2.2.6), the right side of (2.4.30) can be identified as the right side of (2.2.14) multiplied by N_A. Eq. (2.4.30) can thus be expressed as

$$\frac{c_{H^+}[\frac{f}{vJ_0J} - (c_- - c_{H^+} - c_+)]}{(c_- - c_{H^+} - c_+)} = N_A K_a, \tag{2.4.31}$$

where

$$N_A K_a = c_{H^+}^{ref} e^{\frac{\gamma_{as}}{k_B T}}. \tag{2.4.32}$$

(2.4.31) can, by inserting (2.4.12 -2.4.13), be rewritten:

$$\begin{aligned} &\left(1 + \frac{v\bar{c}_+}{v\bar{c}_{H^+}}\right)(vc_{H^+})^3 + \left[\frac{f}{J_0J} + vN_AK_a\left(1 + \frac{v\bar{c}_+}{v\bar{c}_{H^+}}\right)\right](vc_{H^+})^2 \\ &- v\bar{c}_{H^+}\, v\bar{c}_-(vc_{H^+}) - vN_AK_a \cdot v\bar{c}_{H^+}\, v\bar{c}_- = 0. \end{aligned} \tag{2.4.33}$$

This is a cubic equation with the following coefficients:

$$a = 1 + \frac{v\bar{c}_+}{v\bar{c}_{H^+}} \tag{2.4.34}$$

$$b = \left[\frac{f}{J_0J} + vN_AK_a \cdot a\right] \tag{2.4.35}$$

$$c = -v\bar{c}_{H^+}\, v\bar{c}_- \tag{2.4.36}$$

$$d = -vN_AK_a \cdot v\bar{c}_{H^+}\, v\bar{c}_-. \tag{2.4.37}$$

The solution will take the same form as for the anionic case and can be found through (2.4.24-2.4.26). For cationic association the non-poroelastic contribution takes the form

$$U_2 = U_{ion} + U_{as}. \tag{2.4.38}$$

Inserting (2.4.12-2.4.13) into (2.4.6) and (2.4.8) yields

$$
\begin{aligned}
U_{ion} =& k_B T J_0 J \left\{ c_{H^+} \ln\left(\frac{c_{H^+}}{c_{H^+}^{ref}}\right) + c_+ \ln\left[\frac{\bar{c}_+}{c_+^{ref}}\left(\frac{\bar{c}_{H^+}}{c_{H^+}^{ref}}\right)^{-1}\frac{c_{H^+}}{c_{H^+}^{ref}}\right] \right. \\
& \left. + c_- \ln\left[\frac{\bar{c}_-}{c_-^{ref}}\frac{\bar{c}_{H^+}}{c_{H^+}^{ref}}\left(\frac{c_{H^+}}{c_{H^+}^{ref}}\right)^{-1}\right] - c_{H^+}\left(1 + \frac{\bar{c}_+}{\bar{c}_{H^+}} + \frac{\bar{c}_{H^+}\,\bar{c}_-}{c_{H^+}^2}\right)\right\}
\end{aligned}
\tag{2.4.39}
$$

and

$$
\begin{aligned}
U_{as} &= k_B T \cdot J_0 J \left[c_{AH^+} \ln\left(\frac{N_A K_a}{c_{H^+}^{ref}}\frac{c_A c_{H^+}}{c_A c_{H^+}}\frac{c_{AH^+}}{c_{AH^+}+c_A}\right) \right. \\
&\quad \left. + c_A \ln\left(\frac{c_A}{c_{AH^+}+c_A}\right)\right] \\
&= k_B T \cdot J_0 J \left[c_{AH^+} \ln\left(\frac{N_A K_a c_{AH^+}}{c_{H^+} c_A}\right) + c_{AH^+} \ln\left(\frac{c_{H^+}}{c_{H^+}^{ref}}\right) \right. \\
&\quad \left. + (c_{AH^+}+c_A) \ln\left(\frac{c_A}{c_{AH^+}+c_A}\right)\right]
\end{aligned}
\tag{2.4.40}
$$

respectively. The right sides of (2.2.1-2.2.3) can be recognized and substituted for the chemical potentials yielding

$$
\begin{aligned}
U_{ion} =& J_0 J \left[c_+(\mu_+ - \mu_{H^+}) + c_-(\mu_- + \mu_{H^+}) - k_B T \cdot c_{AH^+} \ln\left(\frac{c_{H^+}}{c_{H^+}^{ref}}\right) \right. \\
& \left. - k_B T \cdot c_{H^+}\left(1 + \frac{\bar{c}_+}{\bar{c}_{H^+}} + \frac{\bar{c}_{H^+}\,\bar{c}_-}{c_{H^+}^2}\right)\right]
\end{aligned}
\tag{2.4.41}
$$

and

$$
\begin{aligned}
U_{as} =& J_0 J \left[k_B T \cdot c_{AH^+} \ln\left(\frac{c_{H^+}}{c_{H^+}^{ref}}\right) \right. \\
& \left. + k_B T \cdot c_{AH^+} \ln\left(\frac{N_A K_a c_{AH^+}}{c_{H^+} c_A}\right) + k_B T \frac{f}{J_0 J v} \ln\left(\frac{J_0 J v c_A}{f}\right) \right]
\end{aligned} \tag{2.4.42}
$$

respectively. Inserting (2.4.41-2.4.42) into (2.4.38) yields

$$
\begin{aligned}
U_2 =& \frac{k_B T}{v/J_0} \left[J v c_{AH^+} \ln\left(\frac{v N_A K_a v c_{AH^+}}{v c_{H^+} v c_A}\right) + \frac{f}{J_0} \ln\left(\frac{J_0 J v c_A}{f}\right) \right. \\
& \left. - v c_{H^+} J \left(1 + \frac{v\bar{c}_+}{v\bar{c}_{H^+}} + \frac{v\bar{c}_{H^+}\, v\bar{c}_-}{(v c_{H^+})^2}\right) + c_+(\mu_+ - \mu_{H^+}) + c_-(\mu_- + \mu_{H^+}) \right].
\end{aligned} \tag{2.4.43}
$$

The reference concentrations are still represented through (2.2.1-2.2.3).

2.4.3 Finding the initial swelling of the reference state

Eq. (2.1.20) gives an expression for the stress component σ_{11}:

$$
\sigma_{11} = \frac{N k_B T}{J_0 J}(B_{11} - 1) - (\Pi_{sol} + \Pi_{ion}), \tag{2.4.44}
$$

where the osmotic pressure for mixing of the solvent and for the electrochemic potential is given by

$$
\Pi_{sol} = -\frac{k_B T}{v} \left[\ln\left(1 - \frac{1}{J_0 J}\right) + \frac{1}{J_0 J} + \frac{\chi}{(J_0 J)^2} \right] \tag{2.4.45}
$$

and

$$
\Pi_{ion} = k_B T (c_{H^+} + c_+ + c_- - \bar{c}_{H^+} - \bar{c}_+ - \bar{c}_-) \tag{2.4.46}
$$

respectively. In the homogeneous reference state $J = 1$ and $B_{11} = \lambda_0^2 = J_0^{2/3}$. (2.4.44) then takes the form

$$
\sigma_{11} = \frac{k_B T}{v} \cdot \frac{v N}{J_0}(J_0^{2/3} - 1) - (\Pi_{sol,0} + \Pi_{ion,0}) = 0, \tag{2.4.47}
$$

where

$$
\Pi_{sol,0} = -\frac{k_B T}{v} \left[\ln\left(1 - \frac{1}{J_0}\right) + \frac{1}{J_0} + \frac{\chi}{J_0^2} \right] \tag{2.4.48}
$$

and

$$\Pi_{ion,0} = \frac{k_B T}{v}\left[vc_{H^+} - v\bar{c}_{H^+} + \left(\frac{v\bar{c}_{H^+}}{vc_{H^+}}v\bar{c}_- - v\bar{c}_+\right)\left(1 - \frac{vc_{H^+}}{v\bar{c}_{H^+}}\right)\right], \quad (2.4.49)$$

after inserting the Donnan equations (2.4.12-2.4.13). Given the initial conditions and material model, vc_{H^+} can be found as described above. Then it is just a matter of solving (2.4.47) numerically for J_0 in order to find the initial swelling of the network in the reference state. It is important to note that this approach is only valid if the reference state is homogeneous ($\mathbf{F}_{tot} = \mathbf{F}_0$) and stress-free ($\boldsymbol{\sigma} = 0$). It will not yield a valid solution if the geometry is arbitrarily constrained as in the current approach, where a hemiellipsoidal network is being covalently attached to an optical fiber. It is however assumed that the geometrical constraints are first enforced when the system has reached the reference state.

2.5 Implementing the cationic model

Inserting (2.1.21) into (2.4.9) yields:

$$\begin{aligned} U_1 = U_{str} + U_{mix} = \frac{k_B T}{v/J_0}\Bigg\{ & \frac{1}{2}Nv\left[\frac{1}{\lambda_0}J^{2/3}\bar{I}_1 - \frac{3}{J_0} - \frac{2}{J_0}\log(J_0 J)\right] \\ & - \left[(J - \frac{1}{J_0})\log(\frac{J}{J - \frac{1}{J_0}}) + \frac{\chi}{J_0^2 J}\right]\Bigg\}. \end{aligned} \quad (2.5.1)$$

In order to express the free energy density function in terms of the external salt concentrations instead of the chemical potentials, a suitable Legendre transformation, $\hat{U}$, can be used[1]:

$$\begin{aligned} \hat{U} &= U - J_0 J\left[c_-(\mu_- + \mu_{H^+}) + c_+(\mu_+ - \mu_{H^+})\right] - \mu_S C_S \\ &= U_1 + \hat{U}_2, \end{aligned} \quad (2.5.2)$$

where

$$\hat{U}_2 = U_2 - J_0 J\left[c_-(\mu_- + \mu_{H^+}) + c_+(\mu_+ - \mu_{H^+})\right] - \mu_S C_S. \quad (2.5.3)$$

Inserting (2.4.43), (2.2.4) and (2.2.7) into (2.5.3) yields

$$\begin{aligned}\hat{U}_2 = k_B T \Bigg[& J_0 J \ln\left(\frac{N_A K_a c_{AH^+}}{c_{H^+} c_A}\right) c_{AH^+} + \frac{f}{v} \ln\left(\frac{J_0 J c_A v}{f}\right) \\ & - J_0 J \left(1 + \frac{\bar{c}_+}{\bar{c}_{H^+}} + \frac{\bar{c}_{H^+}\, \bar{c}_-}{(c_{H^+})^2}\right) c_{H^+} \\ & + (J_0 J - 1)(\bar{c}_{H^+} + \bar{c}_+ + \bar{c}_-)\Bigg] .\end{aligned} \tag{2.5.4}$$

This can be expressed as

$$\begin{aligned}\hat{U}_2 = \frac{k_B T}{v/J_0} \Bigg[& J \ln\left(\frac{v N_A K_a v c_{AH^+}}{v c_{H^+} v c_A}\right) v c_{AH^+} + \frac{f}{J_0} \ln\left(\frac{J_0 J v c_A}{f}\right) \\ & - J \left(1 + \frac{v\bar{c}_+}{v\bar{c}_{H^+}} + \frac{v\bar{c}_{H^+}\, v\bar{c}_-}{(v c_{H^+})^2}\right) v c_{H^+} \\ & + \left(J - \frac{1}{J_0}\right)(v\bar{c}_{H^+} + v\bar{c}_+ + v\bar{c}_-)\Bigg] .\end{aligned} \tag{2.5.5}$$

As shown in [1] the chosen Legendre transformation makes $\hat{U}$ describe the material in terms of a hyperelastic solid, and it can thus be implemented in the user subroutine Uhyper in *ABAQUS*.

2.5.1 Implementing $\hat{U}$ in a user subroutine

The user subroutine Uhyper requires U to be hyperelastic and the initial stresses to be zero[7]. The subroutine gets $\bar{I}_1$ and J as input from the FE-program, and needs the characteristic material parameters together with J_0, to enforce homogeneous initial conditions, as further input. This was passed to Uhyper through the *PROPS* vector. What needs to be implemented is according to the *ABAQUS* documentation the free energy density function for the hyperelastic material, and its first and second derivatives with respect to $\bar{I}_1$ and J.

U can be implemented in the user-subroutine UHYPER by solving the unknown quantity vc_{H^+} and coding U with its first and second derivatives. Using that information, ABAQUS will be able to calculate the stresses. In order to implement the free energy density functions in a user subroutine they were normalized by

$$Norm = \frac{k_B T}{v/J_0}. \tag{2.5.6}$$

To enforce the hyperelastic requirement, $\hat{U}$ needed to be implemented instead of U. The normalized contributions to the free energy density function thus takes the form

$$\begin{aligned} U_1^* = \frac{1}{2}Nv\left[\frac{1}{\lambda_0}J^{2/3}\bar{I}_1 - \frac{3}{J_0} - \frac{2}{J_0}\log(J_0 J)\right] \\ -(J-\frac{1}{J_0})\log(\frac{J}{J-\frac{1}{J_0}}) - \frac{\chi}{J_0^2 J} \end{aligned} \tag{2.5.7}$$

$$\begin{aligned} \hat{U}_2^* =& vc_{AH^+}\ln\left(\frac{vN_A K_a vc_{AH^+}}{vc_{H^+}vc_A}\right) + \frac{f}{J_0}\ln\left(\frac{J_0 J vc_A}{f}\right) \\ &- vc_{H^+}J\left(1 + \frac{v\bar{c}_+}{v\bar{c}_{H^+}} + \frac{v\bar{c}_{H^+}\,v\bar{c}_-}{(vc_{H^+})^2}\right) \\ &+ \left(J - \frac{1}{J_0}\right)(v\bar{c}_{H^+} + v\bar{c}_+ + v\bar{c}_-)\,. \end{aligned} \tag{2.5.8}$$

$\hat{U}$ was implemented in two separate steps. First U_1^* was coded together with its derivatives, and then $\hat{U}_2^*$ was implemented. While finding the derivatives of U_1^* was quite straightforward, $\hat{U}_2^*$ is dependent of several parameters such as $vc_{H^+}(J)$, $vc_{AH^+}(vc_{H^+})$ and $vc_A(vc_{AH^+})$. The chain rule was therefore extensively used in the derivation of the derivatives of $\hat{U}_2^*$, where an important part was to find the derivatives of $vc_{H^+}(J)$.

2.5.2 Derivatives of $vc_{H^+}(J)$

The case where (2.4.24) is complex must be handled in the code in terms of an if-else structure testing whether $q^2 - p^3$ is negative. When negative, the algorithm for calculating vc_{H^+} used in [1] was adopted. Due to the logical structure of this algorithm, the derivatives of vc_{H^+} could not be found directly. However, they could be found by using the derivative of the cubic equation:

$$Q(J) \equiv a\cdot[vc_{H^+}(J)]^3 + b(J)\cdot[vc_{H^+}(J)]^2 + c\cdot vc_{H^+}(J) + d \equiv 0 \tag{2.5.9}$$

where only the coefficient b is dependent of J.

$$\begin{aligned} \frac{\partial Q}{\partial J} &= \frac{\partial vc_{H^+}}{\partial J}\left[3a\cdot(vc_{H^+})^2 + 2b(J)\cdot vc_{H^+} + c\right] + (vc_{H^+})^2\cdot\frac{\partial b(J)}{\partial J} \\ &= \frac{\partial vc_{H^+}}{\partial J}\cdot u(J) + (vc_{H^+})^2\cdot\frac{\partial b(J)}{\partial J} = 0, \end{aligned} \tag{2.5.10}$$

where

$$u(J) = 3a \cdot [vc_{H^+}(J)]^2 + 2b(J) \cdot vc_{H^+}(J) + c. \tag{2.5.11}$$

Rearranging (2.5.10) expresses $\frac{\partial vc_{H^+}}{\partial J}$ explicitly:

$$\frac{\partial vc_{H^+}}{\partial J} = -\frac{[vc_{H^+}(J)]^2}{u(J)} \cdot \frac{\partial b(J)}{\partial J}. \tag{2.5.12}$$

Since all the variables on the right side of (2.5.12) can be readily calculated, this expression can be implemented directly in the user subroutine. To find $\frac{\partial^2 vc_{H^+}}{\partial J^2}$, the chain rule can be applied on (2.5.12), and the right side of (2.5.12) can be recognized as an implicit term in the result and then be substituted by $\frac{\partial vc_{H^+}}{\partial J}$. A similar approach can also be used to find the third derivative of vc_{H^+}.

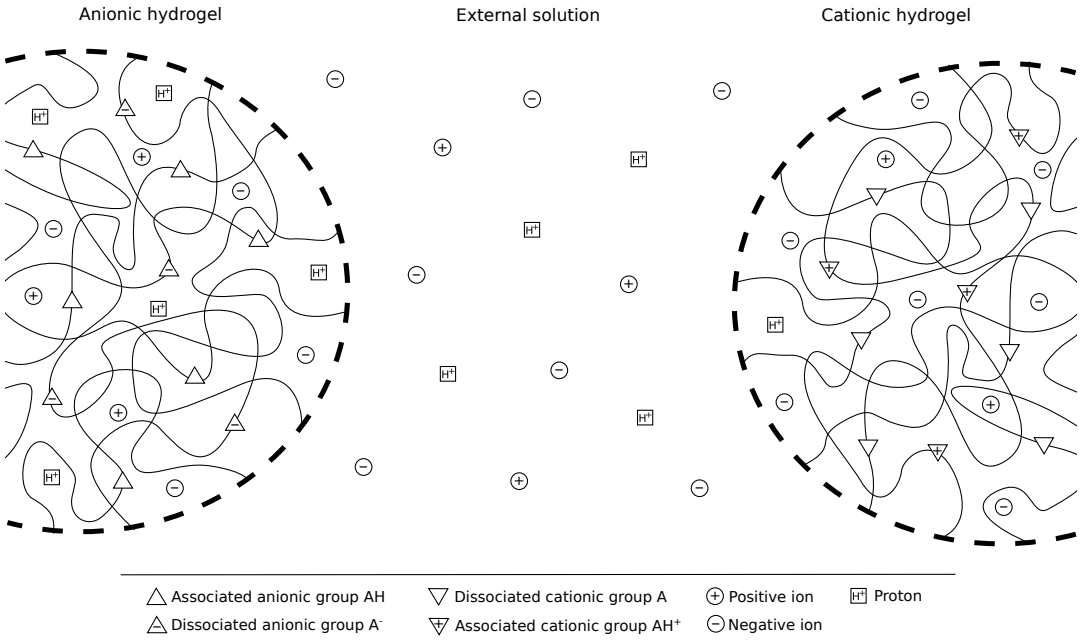

Figure 2: Schematic of an anionic polymer network and the external solution. The polymer network contains fixed ionizable groups and charges, while both network and external solution contains the solvent and all types of free ions, and fulfills electroneutrality. For a cationic network, the fixed species in the network will take a different form.

3 Simulation setup

3.1 Geometry and parameters

The parameters used to describe the properties and geometry of the hydrogel sensor are defined in table 4. The sensor being modeled is a hemispheroidal hydrogel, covalently attached to an optical fiber. The main component of the network is Acrylamide monomers with Bisacrylamide as a crosslinker. A fraction of the monomers also contain ionizable groups that will make the swelling depend on pH and I. An optical micrograph of the geometry is shown in figure 3.

Table 4: Parameters defining the properties and geometry of the hydrogel network.

vN	1	$1/vN$ is the number of monomers per polymer chain
χ	1	Flory-Huggins parameter
f	1	Fraction of monomers with ionizable group
$\mathrm{p}K_a$	1	Logarithmic acid dissociation constant
pH_0	1	pH value at polymerization
I	M	Salt concentration, or ion strength, in the external solution
I_0	M	Ion strength in the external solution at polymerization
λ_0	1	Initial, stress-free principal stretch
L_0	m	Initial, stress-free axial/longitudinal thickness
L_g	m	Constrained, deformed axial thickness
L_{opt}	m	Optical length of the deformed axial thickness
R_f	m	Radius of the optical fiber
L_f	m	Axial length of the optical fiber included in the simulation
L_s	m	Shell thickness
f_s	1	Relative shell thickness
L_S	m	Arc length of the outer hydrogel surface

The axial optical length L_{opt} of the attached hydrogel is found by sending light through the fiber and comparing the reflection in the interface between fiber and gel with the reflection in the interface between gel and solvent. The optical duct for the light can be seen in the center of the optical fiber in figure 3. The diameter of the optical fiber is $2R_f = 125\,\mu\mathrm{m}$, while the initial physical axial length L_0 typically is 50 µm.

Since L_{opt} is measured with the sensor while L_g is retrieved from the simulations, a relation between the lengths must be established. The theory of converting between L_{opt} and L_g of the hydrogel is described in [2]. An approximate relation between the lengths is

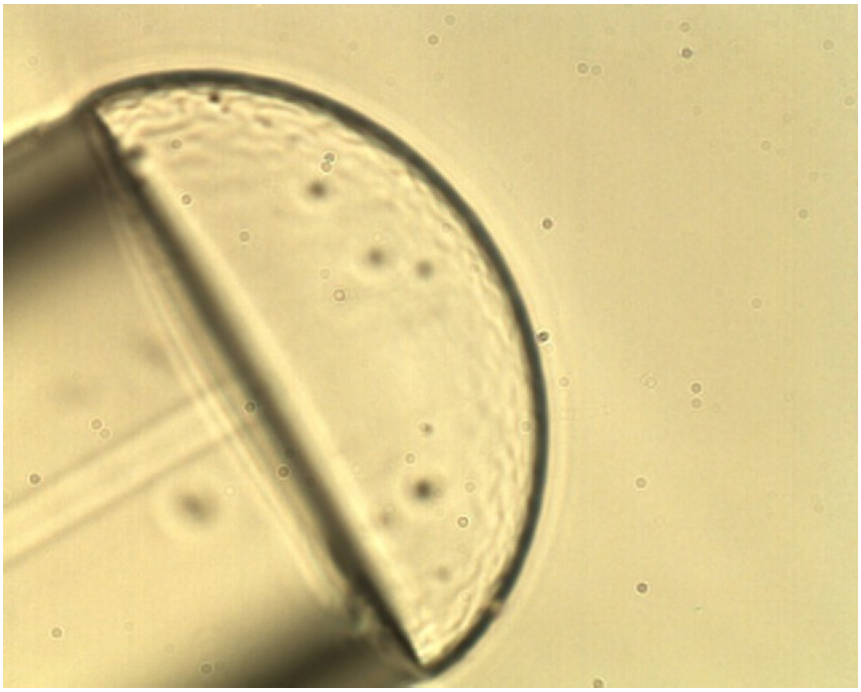

Figure 3: Optical micrograph of hemispherical hydrogel, covalently attached to the end of an optical fiber. Reproduced from [2] with permission. The diameter of the fiber is 125 µm, while L_g is typically 50 µm.

$$L_g \simeq \frac{L_{opt}}{1.33}, \tag{3.1.1}$$

where the refractive index of water, 1.33, is used. (3.1.1) can thus be used in comparison of simulation results with experimental data. The sensor accuracy for L_{opt} is approximately 2 nm. For a hydrogel with $L_g = 50$ µm this yields an error of

$$\delta_{50} \simeq \frac{2\,\text{nm}}{1.33 \cdot 50000\,\text{nm}} \simeq 0.003\%. \tag{3.1.2}$$

It can be seen from the expression that the error will be even smaller for $L_g > 50$ µm. This will often be the case when the hydrogel swells, even for smaller values of L_0.

3.1.1 Geometry of the sensor system

Figure 4 shows the geometry of the hydrogel sensor and the defining lengths implemented in the simulations. R_f is the radius of the fiber and will throughout the simulations be set to 62.5 µm in accordance with the optical micro-

graph in figure 3. L_f is the length of the fiber, and needs to be long enough to enable contact between the outer part of the fiber and the surface of the gel in cases of extreme swelling. Apart from that, it only plays a visal role and needs to be greater than zero. L_S is the surface arc length of the outer hydrogel surface, or the shell. L_s defines the thickness of the shell, that might be attributed different material parameters than the core of the gel to simulate the effects of impregnating the hydrogel. This parameter will for practical reasons be passed to the simulations in terms of the relative shell thickness,

$$f_s = \frac{L_s}{L_0}. \tag{3.1.3}$$

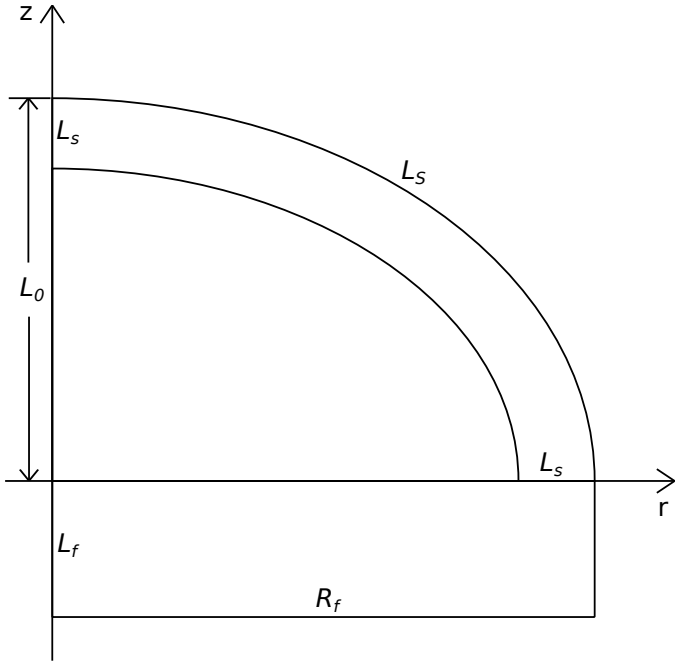

Figure 4: Sketch of the geometry showing the lengths. The coordinates are cylindrical and the longitudinal axis, z, is the symmetry axis.

3.1.2 Materials

See table 5 for the materials used in this section. The gels $AMPSA_1$ and $AMPSA_2$ denotes acrylamide hydrogels where 1.54 mol% and 2.2 mol% respectively of the monomer groups are AMPSA. The gels $DMAPA_3$ and $DMAPA_7$ denotes acrylamide polymer hydrogels where 3 mol% and 7 mol% respectively of the monomer groups are DMAPA. CHIT300 denotes CHIT

with molecular weight of about 300 kDa. AMPSA_{im} denotes AMPSA_2 impregnated with CHIT300.

Table 5: The ionizable groups of monomers in the polymer network.

AMPSA	2-Acrylamido-2-methylpropanesulfonic Acid $\text{p}K_a = 2.0$; $SO_3H \rightleftharpoons SO_3^- + H^+$
DMAPA	N-(3-dimethylaminopropyl) acrylamide $\text{p}K_a = 9.5$; $NH + H_2O \rightleftharpoons NH_2^+ + OH^-$
CHIT	Chitosan $\text{p}K_a = 6.5$; $NH + H_2O \rightleftharpoons NH_2^+ + OH^-$

3.1.3 Parameter values

The parameter values in table 6 are partly retrieved from papers and partly being estimated. For the AMPSA gels, $\text{p}K_a$, f, pH_0, I_0 and L_0 could be found in [8], while the rest had to be estimated using the experimental data they provided. For the DMAPA gels only f, pH_0 and I_0 could be found in [2], and the rest of the parameters had to be estimated from the provided experimental data. The estimation process is reproduced in section 4.1.

Table 6: The gels and parameters used in the simulation setup. Some parameters for the DMAPA and AMPSA gels were provided from [2] and [8] respectively, together with experimental data to estimate the remaining parameters.

	Chemical parameters				Geometrical parameters			
Gel	vN	χ	$\text{p}K_a$	f	pH_0	I_0 [mM]	L_0 [µm]	λ_0
AMPSA_1	3.4e-3	0.37	2.0	0.0154	5	150	50.79	2.2754
AMPSA_2	3.0e-3	0.37	2.0	0.0220	5	150	42.81	2.3379
DMAPA_3	4.9e-2	0.41	9.5	0.03	6.7	50	50.0	1.5598
DMAPA_7	5.1e-2	0.41	9.5	0.07	6.7	50	50.0	1.6743

These parameter values govern the hydrogel swelling behavior together with the free energy density function U.

3.2 Calculation and simulation

This section will be focusing on the simulation setup and the representation of the simulation results. Table 7 introduces the parameters relevant for setting up the simulations, while tables 8 and 9 presents the parameters used

to present the results in section 4. The swelling capacity describes the axial deformation in relation to the initial geometry of the polymer network:

$$\Delta L = L_g - L_0 \tag{3.2.1}$$

$$\Delta L^{exp} = L_g^{exp} - L_0. \tag{3.2.2}$$

$$\Delta L^{im} = L_g^{im} - L_0. \tag{3.2.3}$$

Table 7: Parameters used in representation of simulation results.

L_g^{free}	m	Unconstrained axial deformation
L_g^{num}	m	L_g^{free}, obtained from numerical calculations
L_g^{im}	m	Constrained axial deformation of impregnated gel
L_g^{exp}	m	Constrained axial deformation from experimental data
ΔL	m	Swelling capacity for constrained axial deformation
ΔL^{exp}	m	Swelling capacity for L_g^{exp}
ΔL^{im}	m	Swelling capacity for L_g^{im}
ϵ	1	Strain: see table 8
ϵ_r	1	Relative swelling capacity
δ	1	Relative deviation: see table 9
ξ	1	Square of residuals
w	1	Weight function
E_S	1	Number of simulation grid elements along the gel surface, L_S
E_S^*	1	Approximate number of elements along L_S
E_f	1	Number of elements in the optical fiber along R_f
$E_{s,min}$	1	Minimum number of elements along thickness of the shell

ΔL is useful when comparing swelling curves from gels with the same chemical parameter values but with deviating geometries. The strains in table 8 describe the relative difference between one state and another state used as a reference. Most notable is ϵ_c, which is gives a relative comparison between constrained swelling through L_g and free swelling through L_g^{free}.

In addition to the strains in table 8 the relative swelling capacity, ϵ_r, can also be expressed:

$$\epsilon_r = \frac{\Delta L - \Delta L^{im}}{\Delta L}. \tag{3.2.4}$$

Table 9 shows the relative deviations. Rather than comparing one state with a different one, δ compares two representations of the same state and is thus a measure of the relative error between the representations. The most important one is δ_e, which is the error of the simulation results compared with experimental data.

Table 8: Strain definitions. The strains can be understood as a relative difference between one state and another state used as a reference.

Strain	Definition
Volumetric	$\epsilon_v = \frac{J-J_0}{J_0}$
Longitudinal	$\epsilon_l = \frac{L_g-L_0}{L_0}$
Constrictional	$\epsilon_c = \frac{L_g-L_g^{free}}{L_g^{free}}$
Impregnational	$\epsilon_s = \frac{L_g^{im}-L_g}{L_g}$

Table 9: Relative deviations. The deviations represents the error of one representation of a data set compared with another.

Relative deviation	Definition
from experimental data for L_g	$\delta_e = \frac{L_g-L_g^{exp}}{L_g^{exp}}$
from numerical calculations or L_g^{free}	$\delta_n = \frac{L_g^{free}-L_g^{num}}{L_g^{num}}$
from numerical calculations for J^{free}	$\delta_{n,v} = \frac{J^{free}-J^{num}}{J^{num}}$

3.2.1 Simulation setup

Table 10 shows geometrical parameters used to define the geometry of the simulation models throughout the simulations. The true number of grid elements along the hemispheroidal surface of the gel, E_S, will deviate from the desired number of elements, E_S^*, due to an approximation of hemispheric gel surface in calculating the mesh seed needed to achieve E_S. The difference between E_S and E_S^* is small, however. As shown in section 4.1.1, even a moderate difference would have been of no practical consequence.

Table 10: Fixed geometrical parameter values defining the geometry of a simulation model.

R_f [µm]	L_f	E_S^*	E_f
62.5	$\frac{1}{3}R_f$	30	9

The number of grid elements along the fiber radius, E_f, is only a visual parameter, as the elements in the fiber part of the model normally don't experience any forces from the gel. The movement restrictions on the hydrogel from the fiber is enforced by restricting all the nodes of the hydrogel along the fiber-gel interface. The fiber elements will only experience forces if the

hydrogel swells sufficiently to allow the outer surfaces of the fiber and gel to make contact. It is thus only required that $E_f \geq 1$, and the number of elements along L_f will be a third of E_f, rounded up.

Table 11 shows a set of gels with geometric parameters to complement the values in table 10. When $E_{s,min}$ is set to 1, the mesh will have equal resolution in core and the shell of the gel, and should thus be done in simulations where the effects of impregnation are not considered.

Table 11: Parameters defining the geometry of a simulation model for a pair of gels together with the values in table 10.

Gel	L_0 [µm]	f_s	$E_{s,min}$
$AMPSA_1$	50.79	0.15	1
$AMPSA_{im}$	42.81	0.15	5

The simulation models resulting from the parameter values in tables 10 and 11 are given in figures 5 and 6 for $AMPSA_1$ and $AMPSA_{im}$ respectively.

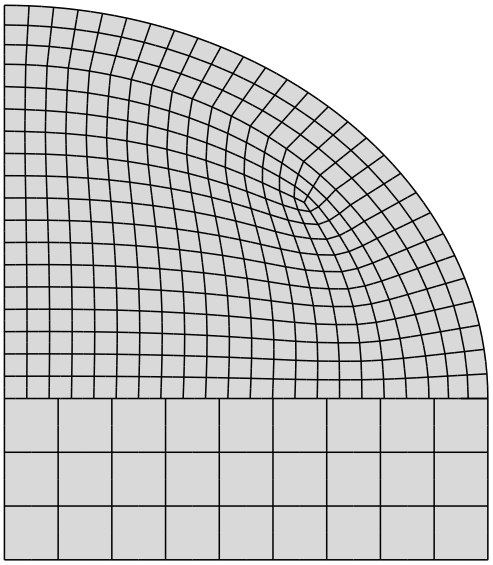

Figure 5: Simulation model of the sensor for $AMPSA_1$. The model is 2D axisymmetrical, with $E_S = 28$ along the surface arc, L_S.

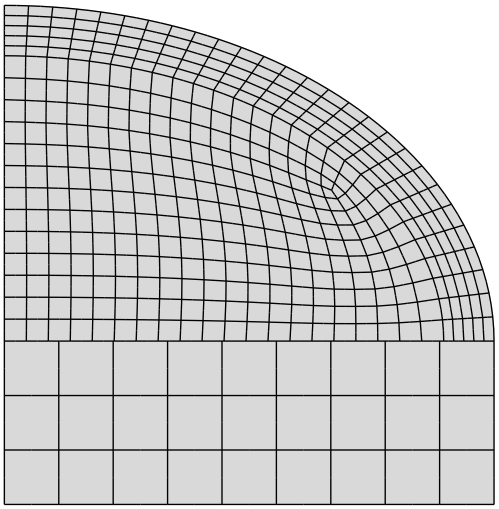

Figure 6: Simulation model of the sensor for AMPSA$_{im}$. The model is 2D axisymmetrical, with $E_S = 27$. The interface between the core and the shell of the gel can clearly be seen where the mesh of the gel becomes denser.

The effect of adjusting $E_{s,min}$ can be seen when comparing the figures. In figure 5 the shell inherits the density of the core, since $E_{s,min}$ is smaller than what the mesh density of the core of the gel would dictate. In figure 6 the value of $E_{s,min}$ is greater than the inherited value, and thus overrides it. Here the boundary between the core and the shell of the gel can be seen clearly, while this interface is obscured in figure 5 due to the homogeneous mesh density of the gel.

Figure 7 illustrates the axisymmetric properties of the simulation setup, and is based on the mesh of AMPSA$_{im}$ in figure 6. The axisymmetric property of the simulation setup ensures that the three dimensional sensor in figure 3 can be modeled using a 2D representation.

In addition to the geometry, the chemical nature of the hydrogel must also be defined in the simulation together with input parameters to tell whether the gel is divided in core and shell, and if the simulation is free or constrained. The parameters needed to define a simulation are listed in table 12 under their respective property vector.

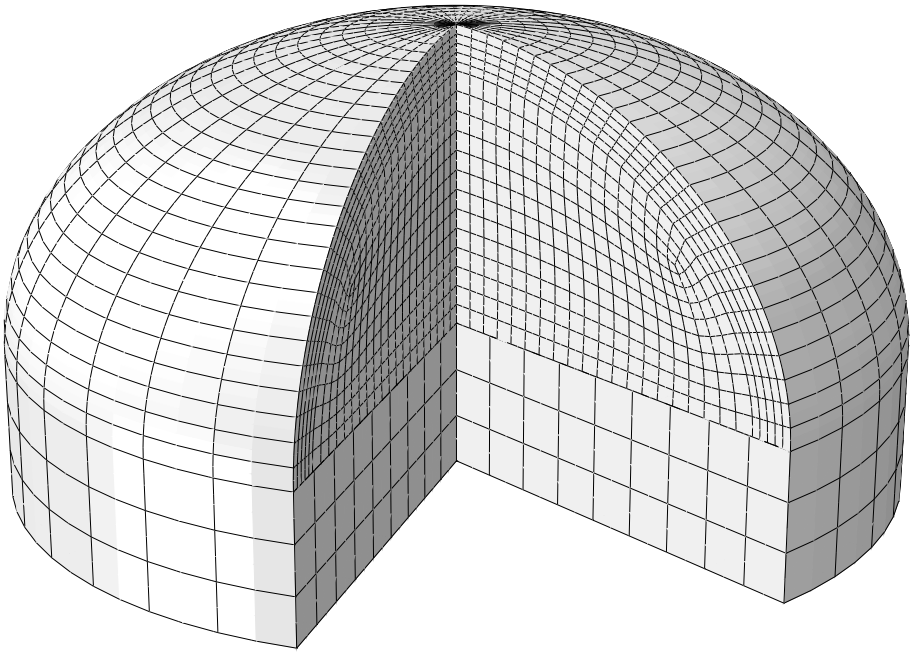

Figure 7: The mesh in figure 6 for AMPSA$_{im}$ swept in a 300 degree angle for illustrational purposes.

Table 12: Property vectors. $AnCat = 1$ for anionic gels and $AnCat = 2$ for cationic gels. The parameters in the $flags$ vector are described in tables 13 and 14.

Property vector	Parameters
gelGeom	$[L_0, R_f, f_s, E_S^*, E_{s,min}, E_f]$
chemProps	$[vN, \chi, \mathrm{p}K_a, f, AnCat]$
flags	$[CoreShell, Cons]$

Table 13: *CoreShell* flag. Describes the chemical properties of the gel together with *chemProps* in table 12

CoreShell	Description
1	Purely anionic gel
2	Purely cationic gel
12	Anionic core, cationic shell
21	Cationic core, anionic shell

Table 14: Constriction flag. Governs whether the simulation is geometrically constrained along the fiber-hydrogel interface.

$Cons$	Description
0	Free swelling
1	Constrained swelling

3.2.2 Parameter estimation setup

As stated in section 3.1.3, not all the characteristic gel parameters were known a priori and had to be estimated by fitting simulation results to experimental data. This fitting was done through iterative nonlinear least square estimation and some relations must thus be established in that regard. ξ is the square of residuals used in the parameter estimation:

$$\xi = \sum_i w_i (L_{g,i} - L_{g,i}^{exp})^2, \tag{3.2.5}$$

where w is a weight function with $w_i = 1$ for the unweighted case. By using $w_i = 1/L_{g,i}^{exp}$, (3.2.5) can be expressed in terms of δ_e:

$$\xi = \sum_i (\delta_{e,i})^2. \tag{3.2.6}$$

The square of residuals can also be expressed in terms of the swelling capacity:

$$\bar{\xi} = \sum_i w_i (\Delta L_i - \Delta L_i^{exp})^2. \tag{3.2.7}$$

The program flow of the parameter estimation process is described in figure 8. The *Matlab* function *lsqnonlin* is initiated with initial parameter values and a specified tolerance. The *Matlab* function *getDiff* will also be passed on to *lsqnonlin* in order for it to retrieve the differences to be minimized. The tolerance includes the maximum number of times *lsqnonlin* can call *getDiff* and the number of decimals to be estimated for the set of variables.

For each iteration, *lsqnonlin* changes the estimation parameters and retrieves a new set of differences between simulation results and experimental data. It then computes the square of residuals from one of the equations (3.2.5-3.2.7), depending on the contents of *getDiff* and form of the experimental data, and attempts to minimize ξ. When the conditions of the estimation reaches the provided tolerance, the estimation process will be terminated and the parameter values corresponding to the minimum value of ξ will be sent back to the initial script.

The simulations themselves were being run in *Abaqus* as described in section 2.5. The parameters defining the geometry and nature of the gel were passed to *Abaqus* from the *Matlab* function *getData*, which also retrieved L_g and J from the FEM-software, enabling *getDiff* to calculate the deviation from L_g^{exp}.

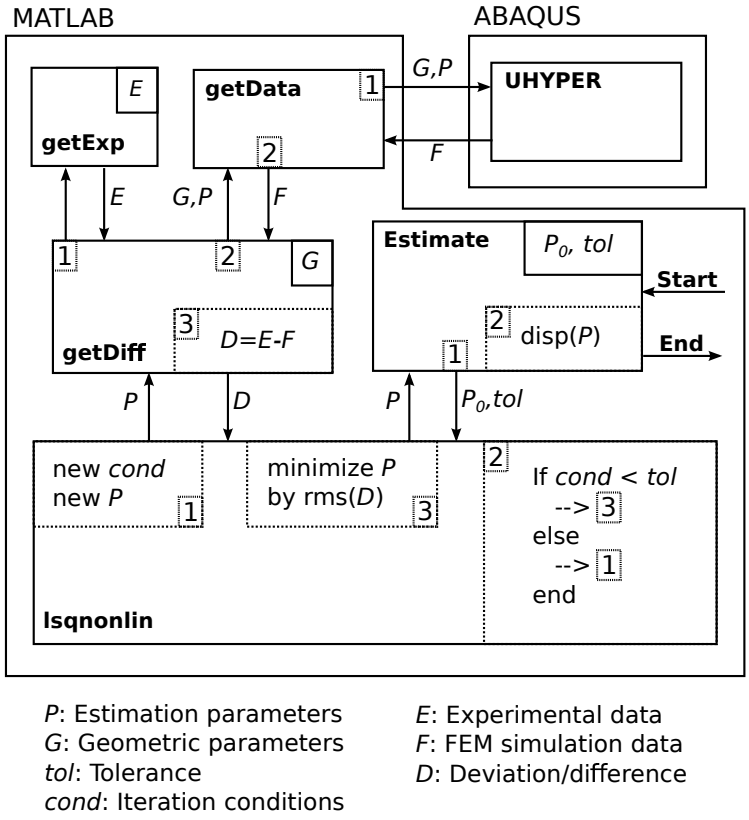

Figure 8: Program flow of the parameter estimation. The solid box in the right top corner of a program lists the constants defined in the routine. The numbers in the dotted boxes indicate the order of which the modules of a program is run, while the arrows represent program calls with input parameters or a return call with output parameters.

4 Results

4.1 Development of method

4.1.1 Determining a feasible mesh resolution

The finite element calculations are numerical and the precision is ultimately restricted by the number of elements in the mesh. Figures 9b and d show how the relative deviation between the steps converges towards zero as E_S is increased.

The difference in L_g when going from $E_S = 22$ to $E_S = 47$ elements along the surface is less than 0.007 percent while the difference from 47 to 92 elements is less than 0.0003 percent. The systematic error of choosing a value of E_S between 22 and 47 elements will thus yield a systematic error of

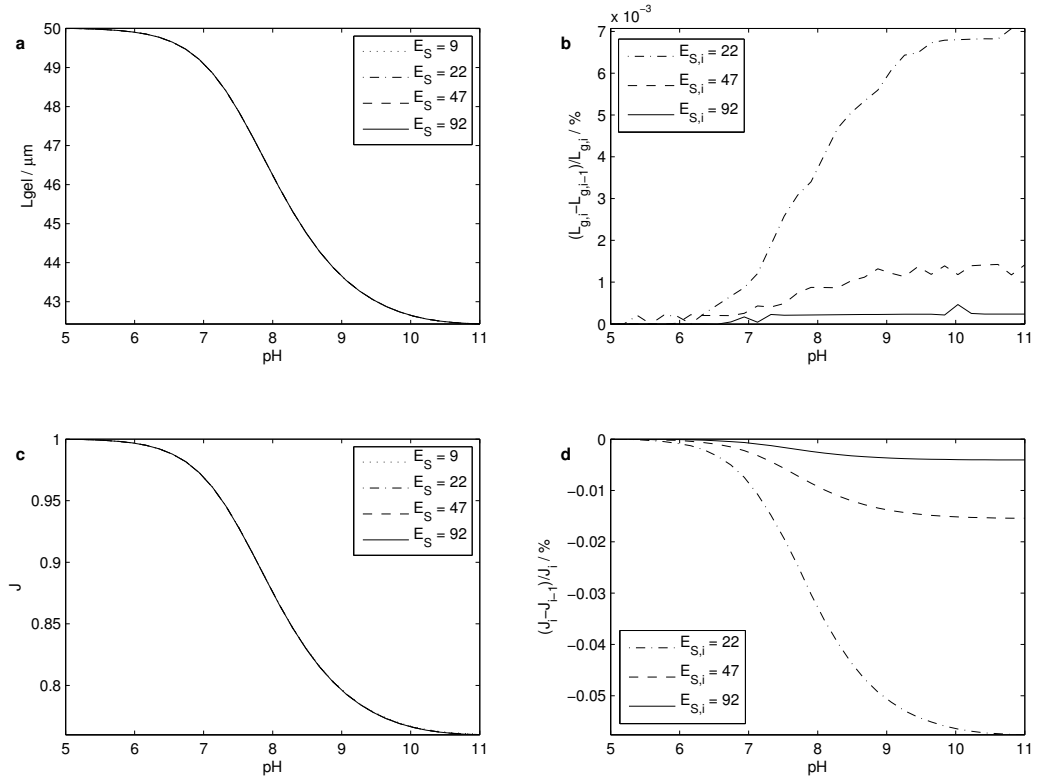

Figure 9: a) Cationic constrained swelling along the symmetry axis using different mesh densities, represented by E_S. **b)** Relative deviation in L_g for a given value of E_S from a) compared to the previous, lower value. **c)** Relative volume change for different mesh densities. **d)** Relative deviation in J for a given value of E_S from c) compared to the previous, lower value. The curves in a) and c) are approximately coinciding.

less than 0.01 percent, without becoming too computationally demanding.

4.1.2 Error of assuming an incorrect reference state

In both [8] and [2] the hydrogels are polymerized and even impregnated[2] at a set of reference conditions often a bit different from the starting conditions of the measurements. The hydrogels are therefore not in a stress-free reference condition at the start of the measurements, which is a crucial criterion for simulations running the UHYPER subroutine in ABAQUS. Figure 10 shows the effect of assuming different start conditions than the true reference conditions as the stress-free state for the $AMPSA_2$ hydrogel.

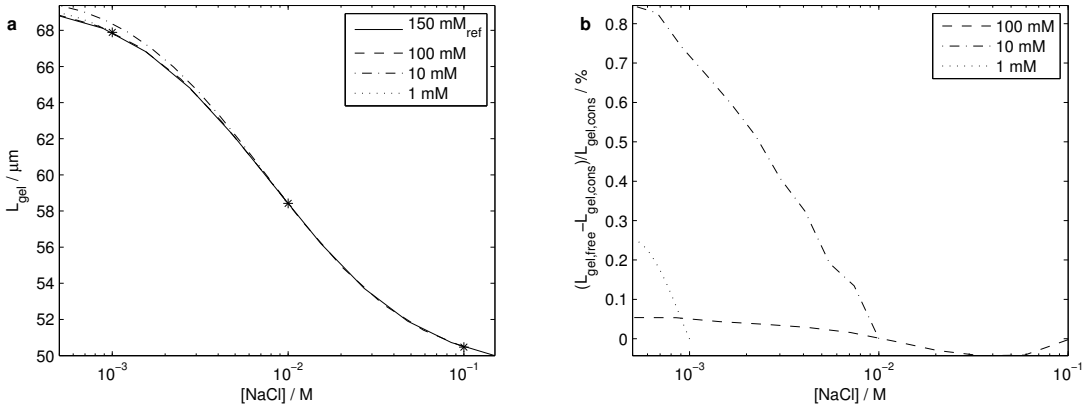

Figure 10: a) The effect of assuming a different reference state than the true stress free state for $AMPSA_2$. The stars indicate the initial conditions of the assumed reference states. **b)** The relative deviation from the reference curve for each of the other lines in a).

The error of choosing $I_0 = 100$ mM as initial condition instead of 150 mM is in figure 10b shown to less than 0.1 percent while the choice of $I_0 = 10$ mM yields an error approaching 0.9 percent. The deviation is smaller again for $I_0 = 1$ mM which is due to the upper plateau of the swelling curve already being reached and the proximity to the end condition, preventing much cumulation of error. How much a deviation in I_0 will impact on the swelling curve is thus dependent on both the deviation itself and the slope of the line.

4.1.3 Limitations of the initial conditions

The limits of the initial conditions of the simulations using *Uhyper* are given in figure 11 and figure 12 for the $AMPSA_2$ and $DMAPA_7$ hydrogels, respectively. For initial conditions outside the indicated ranges, the simulations

were found to not converge and thus abort. The determination of such limits is a useful tool when setting up a more complex simulation series where the initial conditions and simulation range is being varied for simulations featuring different material models.

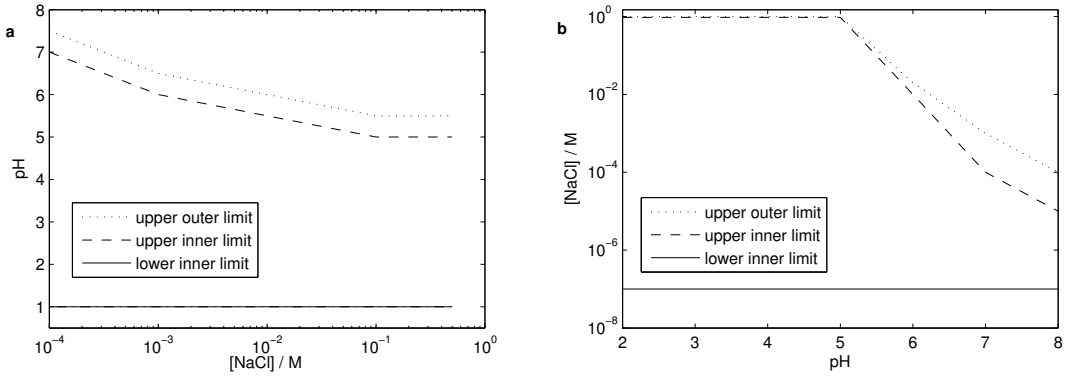

Figure 11: Range of valid $AMPSA_2$ simulation intervals for **a)** I and **b)** pH. For a given value along the x-axis, the limits of the interval can be read out along the y-axis. The inner limits are confirmed to give converging simulations while the outer limits are confirmed not to, when they aren't indicating invalid ranges, such as the 1 M limit. The outer and inner lower limits coincide in a) while the lower outer limit is practically non-existent in b).

It can be seen from the figures that for simulations combining the $AMPSA_2$ and $DMAPA_7$ hydrogels and varying I in the range 3 to 100 mM is bound to conducted around pH 5, and that a simulation varying pH in the range 4 to 6 must be conducted for a value of I just around 10 mM. This implies that any simulations combining $AMPSA_2$ and $DMAPA_7$ will have to be conducted in the range where the anionic gel is fully dissociated and the cationic gel is fully associated, i.e. both gels are fully charged and more sensitive to the concentration of mobile ions. Similar constrictions should be expected for models utilizing other combinations of anionic and cationic materials as well.

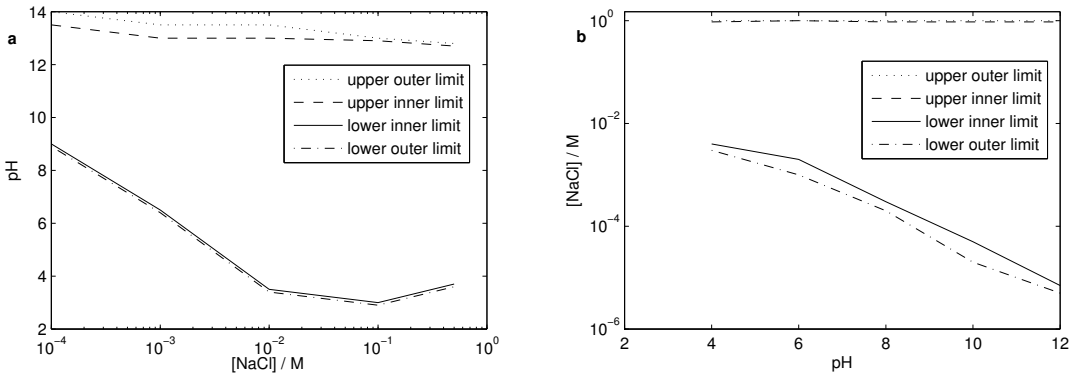

Figure 12: Range of valid $DMAPA_7$ simulation intervals for **a)** I and **b)** pH. For a given value along the x-axis, the limits of the interval can be read out along the y-axis. The inner limits are confirmed to give converging simulations while the outer limits are confirmed not to, when they aren't indicating invalid ranges, such as the 1 M limit.

4.1.4 Estimating characteristic gel parameters

The geometrical properties of a homogeneous hydrogel sensor will generally be known a priori or found in the initial measurements. Some of the chemical parameters can also be known a priori or be experimentally controlled variables, like f, while the rest of them, vN and χ in particular, will have to be estimated by fitting simulation results to available experimental data. The parameters were estimated by running simulations with different parameter values and minimizing χ as described in section 3.2.2.

For anionic hydrogel swelling, data for $AMPSA_1$ and $AMPSA_2$ was provided[8]. The unknown simulation parameters were vN and χ. The initial estimate combined deviations of both $AMPSA_1$ and $AMPSA_2$. The initial and final parameters are listed in table 15.

Table 15: $AMPSA_1$ and $AMPSA_2$ fitted dependently.

Values	vN	χ	$\xi_{1,I}$	$\xi_{2,I}$
Initial	1.0e-3	0.40	-	-
Final	3.14e-3	0.372	9.90e-4	4.35e-4

Independent estimates of the AMPSA-gels were then conducted in order to validate the previous estimate. The results are given in table 16 and corresponds closely with the combined estimates.

χ is in principle the same for the AMPSA-gels while vN might vary slightly. The results in table 16 confirms this and also suggests a value of

Table 16: The AMPSA-gels fitted separately.

Gel	vN	χ	$\xi_{i,I}$
All; Initial	3.1e-3	0.4	-
$AMPSA_1$	3.42e-3	0.370	2.44e-4
$AMPSA_2$	3.02e-3	0.373	7.08e-5

$\chi = 0.37$. Using this value, independent estimates were run to determine vN. These values are given in table 17 and confirms the previous estimate. The resulting chemical parameters were implemented in table 6 and the final fitting is reproduced in figure 16.

Table 17: The AMPSA-gels fitted independently for $\chi = 0.37$.

Gel	vN	$\xi_{i,I}$
All; Initial	3.1e-3	-
$AMPSA_1$	3.42e-3	2.44e-4
$AMPSA_2$	2.98e-3	7.85e-5

4.1.5 DMAPA-estimation

For cationic swelling, [2] provided swelling data for $DMAPA_3$ and $DMAPA_7$ and the unknown simulation parameters were vN, χ, pK_a and L_0. L_0 is unknown due to the swelling data being presented in terms of ΔL in the study. As with the estimation of the AMPSA parameters, an initial fit involving the the combined deviations of the DMAPA gels was conducted, assuming $L_0 = 50.0\,\mu m$. The estimated parameters are given in table 18 and the fitting result is shown in figure 13. It can be noted that the pK_a value appears to be 9.5 as opposed to 8.6[2]. The respective sums of residuals, ξ, should be comparable for the different curve fittings of DMAPA.

Table 18: The DMAPA-gels fitted dependently for both pH and I, assuming $L_0 = 50.0\,\mu m$. The result of the process is reproduced in figure 13.

Values	vN	χ	pK_a	$\xi_{3,pH}$	$\xi_{3,I}$	$\xi_{7,pH}$	$\xi_{7,I}$
Initial	3.0e-2	0.4	8.6	-	-	-	-
Final	5.4e-2	0.43	9.5	1.65	0.05	0.29	1.23

The parameter values from the combined estimate were then used as initial values for independent simulations for each case of swelling. The

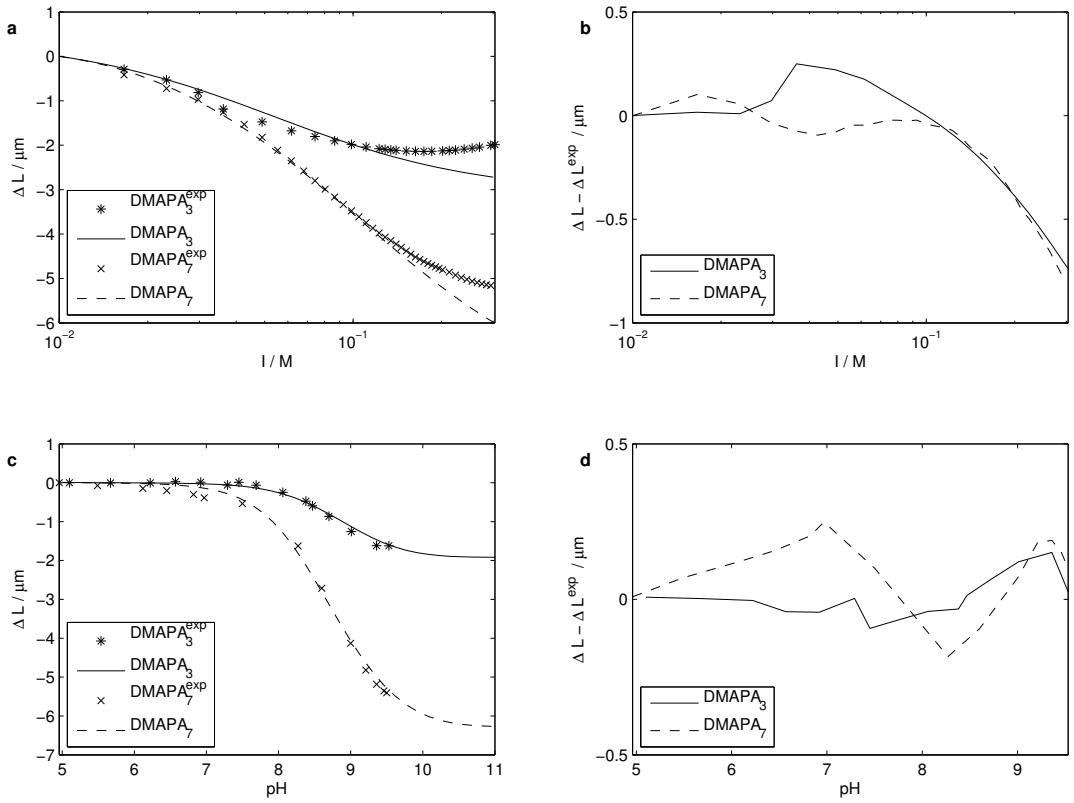

Figure 13: Comparison of experimental data with the simulation results of cationic swelling using the final parameter values in table 18. Swelling capacity compared with experimental data for **a)** increasing ion strength and **c)** increasing pH. **b)** and **d)** show the deviation between the simulations and swelling data in a) and c) respectively.

results are given in table 19 and show that the values are close to the values from the combined estimate, with the exception of $\mathrm{DMAPA}_{3,I}$. The latter estimate reached the upper bound for pK_a and approached the lower bound for L_0.

The values of L_0, with exception of $\mathrm{DMAPA}_{3,I}$, are close to the suggested initial value and are thus assumed to either lay close to the true value or having little effect on the overall estimate. The latter is most likely due to the natural spread in L_0 when polymerizing the gels. Either way; for the rest of the estimates L_0 will be assumed to be 50.0 µm.

The pH simulations indicate a higher χ value than the I simulations and are more consistent with the combined estimate. The I simulations are conducted at pH 6.7 which is far from the pK_a value of about 9.5. They are

Table 19: DMAPA-gels estimated separately. The values indicated in bold have reached or are approaching the upper or lower bounds of the estimation.

Gel	vN	χ	pK_a	L_0[µm]	ξ
All; initial	5.0e-2	0.40	9.5	50	-
DMAPA$_{3,pH}$	5.1e-2	0.44	9.5	48	0.10
DMAPA$_{7,pH}$	4.5e-2	0.37	9.5	47	0.44
DMAPA$_{3,I}$	4.5e-2	0.13	**11.0**	**38**	0.41
DMAPA$_{7,I}$	5.4e-2	0.22	9.4	45	0.48

therefore assumed to be less sensitive to the pK_a than the pH simulations. In order to extract the pK_a value, a combined fitting of the two pH series was conducted with a higher resolution than the previous attempts. The results are given in table 20 and clearly indicate that the pK_a value is 9.5 in agreement with table 18.

Table 20: The DMAPA-gels fitted dependently with respect to pH. pK_a was found to be 9.5.

Values	vN	χ	pK_a	$\xi_{3,pH}$	$\xi_{7,pH}$
Initial	5.0e-2	0.40	9.5	-	-
Final	4.80e-2	0.401	9.53	0.041	0.276

Figure 13 shows that the parts of DMAPA$_I$ exceeding 100 mM couldn't be fitted properly by the simulations. DMAPA$_{3,I}$ even display a trend of increasing L_g for increasing I, a phenomena that can't be reproduced by the current theory and material models for neither cationic nor anionic gels. The estimated line of DMAPA$_{3,I}$ clearly cuts through the experimental curve to compensate for this effect. This deviation from the material model might also account for the failure in estimating the parameters for DMAPA$_{3,I}$ in table 19.

The parameters in table 21 were estimated by excluding the parts where $I > 100$ mM. The values are not far from the initial estimate in table 18, but the ξ values are, with the exception of $\xi_{7,pH}$, considerably lower. Note that the values for $\xi_{i,I}$ can't be directly compared between tables 18 and 21 due to the truncation of the data for high ion strength, since the loss of data points will contribute directly to lower the value of ξ.

As with AMPSA, χ is assumed to be equal for the DMAPA-gels. Furthermore, the value of χ seems to be consistent whether or not the data is truncated above $I = 150$ mM, by comparison of tables 20 and 21. By us-

Table 21: The DMAPA-gels fitted dependently for both pH and I, excluding the parts where $I > 100$ mM. χ was found to be 0.41.

Values	vN	χ	$\xi_{3,pH}$	$\xi_{3,I}$	$\xi_{7,pH}$	$\xi_{7,I}$
Initial	5.0e-2	4.0	-	-	-	-
Final	4.69e-2	0.407	0.053	0.216	0.048	0.901

ing the value of $\chi = 0.41$, vN was estimated individually for $DMAPA_1$ and $DMAPA_2$ in table 22.

Table 22: The value of vN was estimated for $DMAPA_3$ and $DMAPA_7$ by combining the deviations with respect to f. The simulations were conducted with $pK_a = 9,5$ and $\chi = 0.41$, excluding the parts where $I > 100$ mM.

Values	vN	$\xi_{i,pH}$	$\xi_{i,I}$
Initial_{All}	4.7e-2	-	-
Final_3	4.88e-2	0.118	0.047
Final_7	5.12e-2	0.721	0.309

The estimated values of vN can only be assumed to be valid for $I < 100$ mM while χ and especially pK_a seems to be more generally valid. The material model is evidently more applicable on DMAPA for pH simulations than for I simulations. The estimated parameter values are incorporated in table 6 together with the ones known a priori, and the final estimates are given in figure 17.

4.1.6 pKa-value

It was observed in figure 13a that the pK_a-value in the simulation deviates much from the midpoint of the swelling curve for varying pH. Figures 14 and 15 show the swelling fraction as a function of pK_a for free and constrained swelling simulations respectively, for both $AMPSA_2$ and $DMAPA_7$. For a solution of ionizable groups, an equal amount of groups will be associated and dissociated at the pK_a-value. If the swelling was proportional with the distribution of associated and dissociated groups, the swelling fraction would thus have been $\frac{1}{2}$ at the pK_a-value.

The figures indicate that this is not the general case for free nor constrained swelling. The swelling fraction is, with the exception of figure 15b, far below the midpoint, implying that the pK_a-value is strongly shifted towards the plateau of minimum swelling. It can also be seen that lower ion strength will increase this shift. It should be noted that the the swelling

fraction is around equilibrium for DMAPA_7 at $I_0 = 50mM$ and $\text{p}K_a = 8.5$, as suggested in [2].

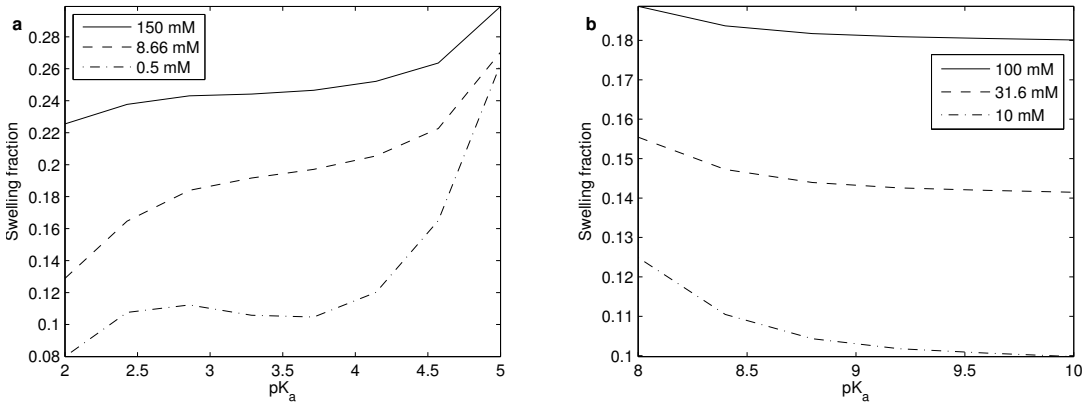

Figure 14: Free swelling. **a)** AMPSA_2, shrunk reference state. **b)** DMAPA_7, swollen reference state.

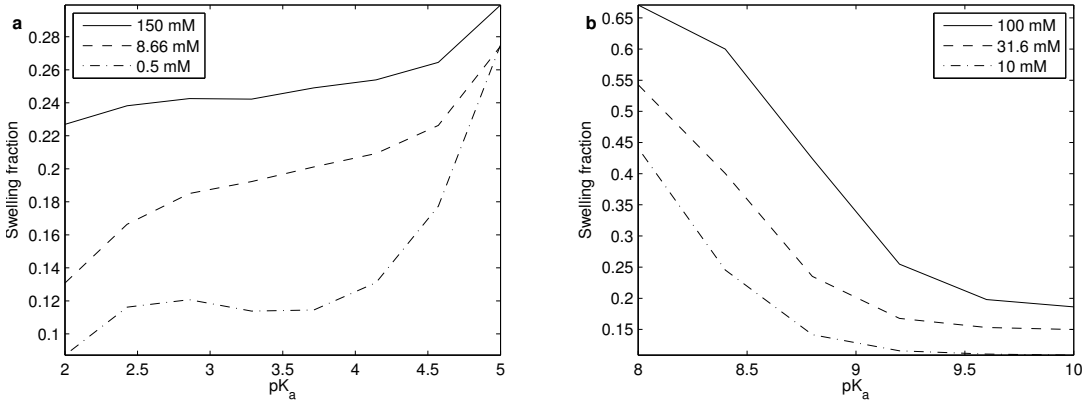

Figure 15: Constrained swelling. **a)** AMPSA_2, shrunk reference state. **b)** DMAPA_7, swollen reference state.

The AMPSA- and DMAPA-simulations are conducted with shrunk and swollen reference states respectively. By comparing figures 14 and 15, it can be seen that the constrictions have little effect on the swelling fraction for the shrunk reference state (a), while they contribute significantly in the case with swollen reference state (b).

4.2 Validation of material models

4.2.1 Comparison to experimental data

Simulations of $AMPSA_1$ and $AMPSA_2$ have been compared with experimental data for the estimated parameters given in table 6. Figure 16a shows the plots together, while figure 16b shows the deviation between simulations and experimental measurements.

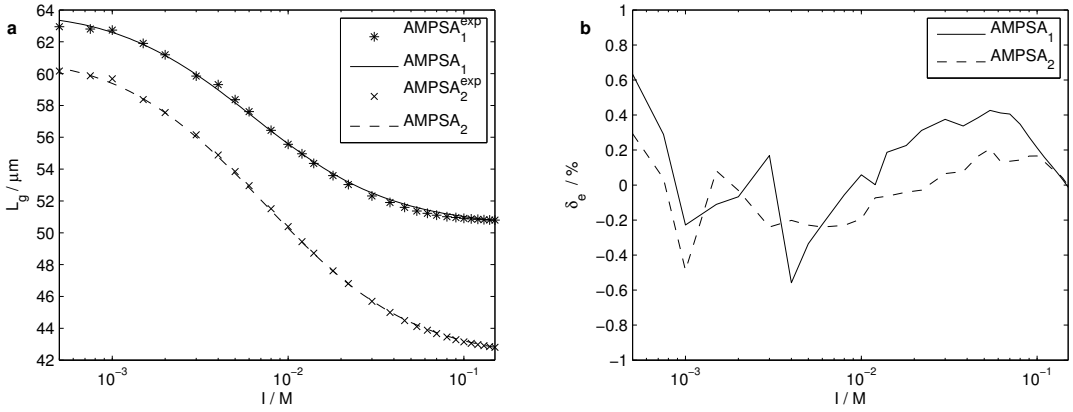

Figure 16: Comparison of constrained simulations with experimental data for anionic swelling. **a)** Comparison with experimental data for decreasing I. **b)** Relative deviation between the simulations and swelling data in a).

The curves show good agreement between the simulations and experimental data. The deviations are less than a percentage from the experimental data at any point and it can be noted that the curves in figure 16b in a broad sense seem to run parallel. This can be an indication of a systematic error either in the experiments or in the theory and simulations.

Figures 17a and 17c shows the comparison of simulation results and experimental data from [2] for increasing ion strength and pH, respectively. The pH-simulations show good agreement with the experimental data. The estimated value of pK_a for fitting the data was found to be 9.5, as opposed to 8.6[2]. This is closer to the bottom plateau of the pH-curves in figure 17c than the midpoint of the slope. The ion strength simulation fails to reproduce the experimental trends for $I < 100$ mM. Figure 17b also shows a strong parallel tendency in this range.

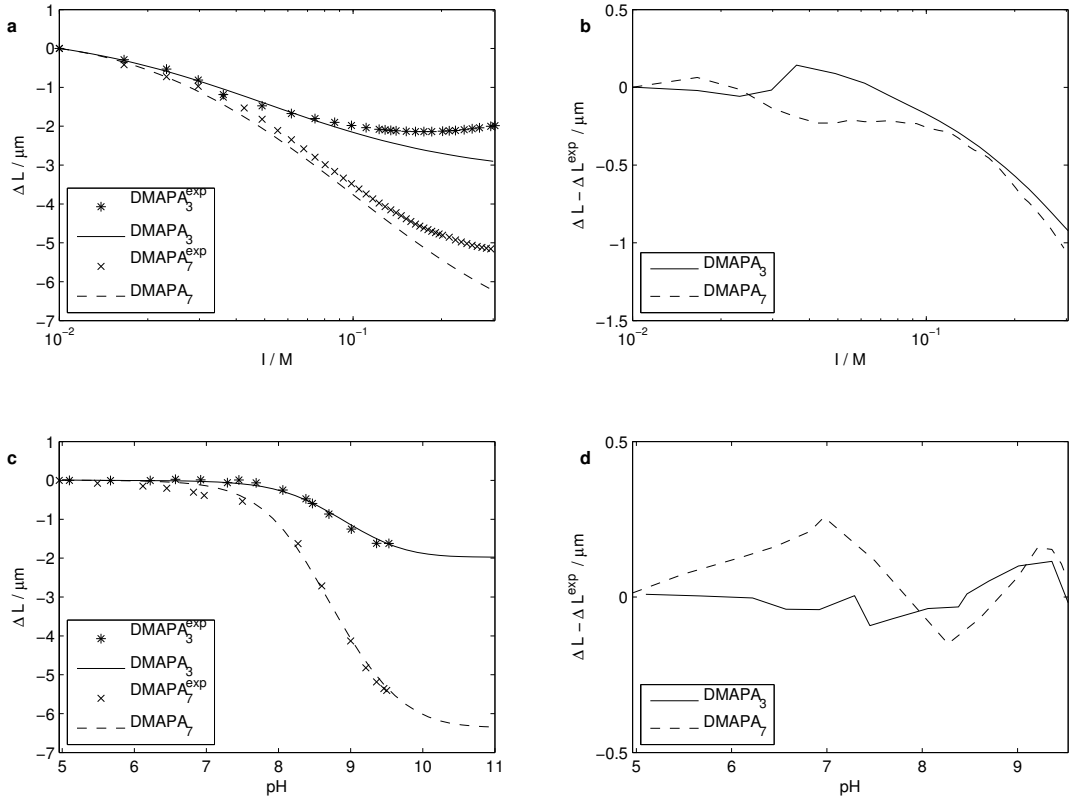

Figure 17: Comparison of constrained simulations with experimental data for cationic swelling. Swelling capacity compared with experimental data for **a)** increasing ion strength and **c)** increasing pH. **b)** and **d)** show the deviation between the simulations and swelling data in a) and c), respectively.

4.2.2 Free swelling

Equation 2.4.47 has been used as a basis for the numerical calculations in this section, by solving it for J_0 and calculating L_g^{free} in accordance with section A.2. It can be seen in figure 18 that the results are equivalent for L_g^{free} and J. δ even have the same form for the two cases, although with different offsets. J will thus be omitted from the rest of the section.

Figure 19 shows L_g^{free} for decreasing pH. The deviation is less than 0.005 percent, with the exception of the initial point of $I = 150$ mM, where the deviation is several times higher than for the other values of I. Figure 20 shows L_g^{free} for increasing pH, and it can be clearly seen that the deviation increases as the simulation approaches the upper pH limit of about 6, indi-

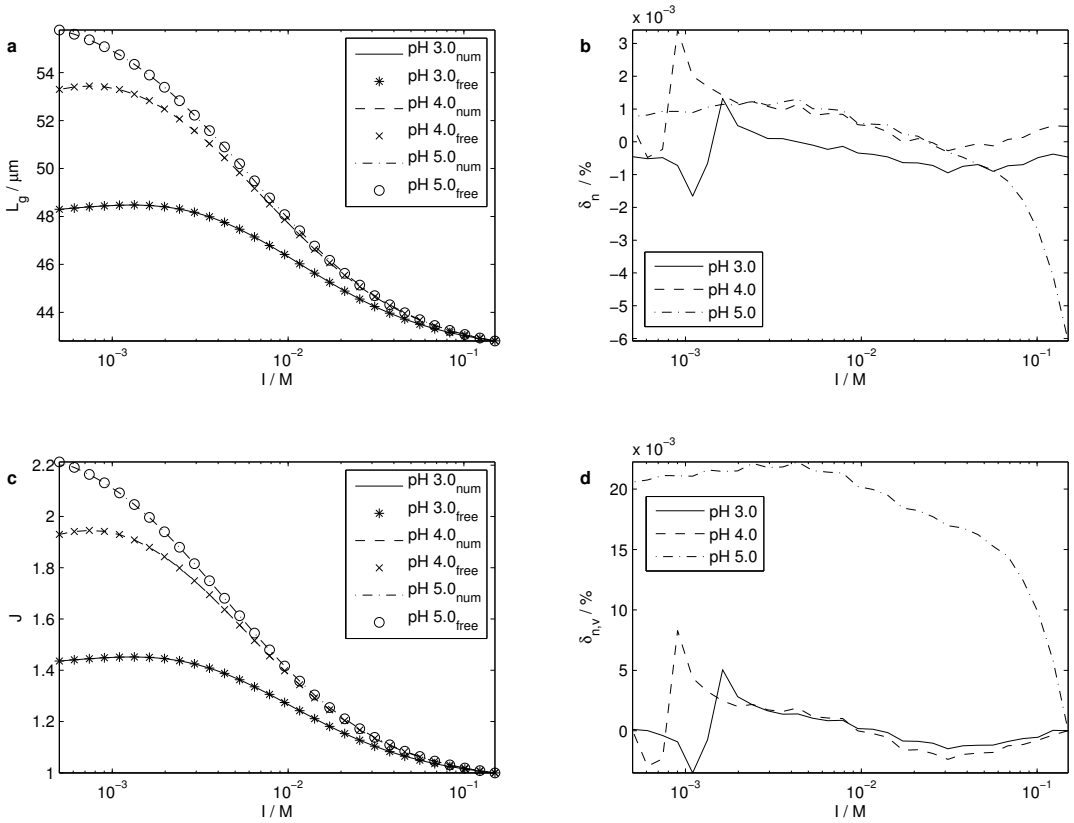

Figure 18: Comparison of unconstrained simulations and numerical calculations for homogeneous swelling when decreasing I for $AMPSA_2$. **a)** and **c)** show the axial deformation and relative change in volume, respectively. **b)** and **d)** are the relative deviations between unconstrained swelling and numerical calculations in a) and c), respectively.

cated in figure 11a. It only shows significantly for $I = 150$ mM, where the upper pH-limit is about 5. This can be an indication on why the deviation for $I = 150$ mM is relatively big in figure 19b, with initial pH 5.

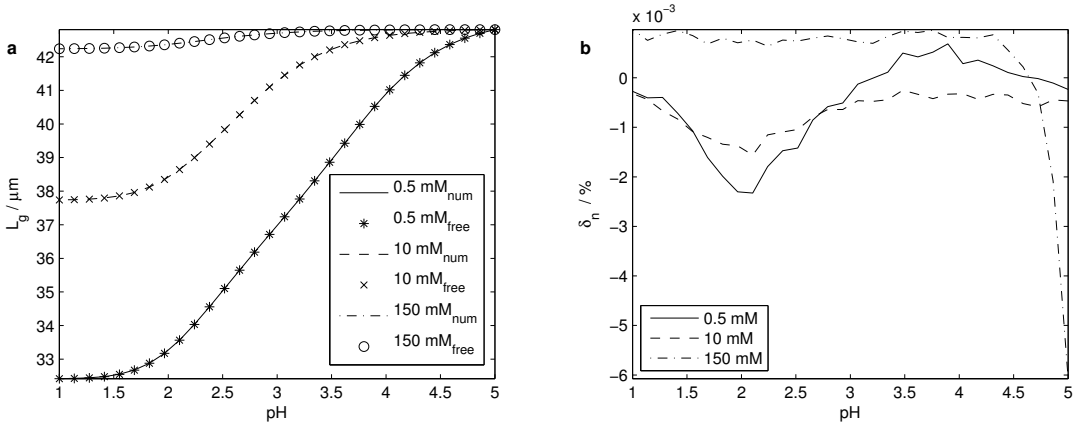

Figure 19: Comparison of unconstrained simulations and numerical calculations for homogeneous swelling when decreasing pH for $AMPSA_2$. **a)** shows the axial deformation while **b)** shows the relative deviation between unconstrained swelling and numerical calculations in a).

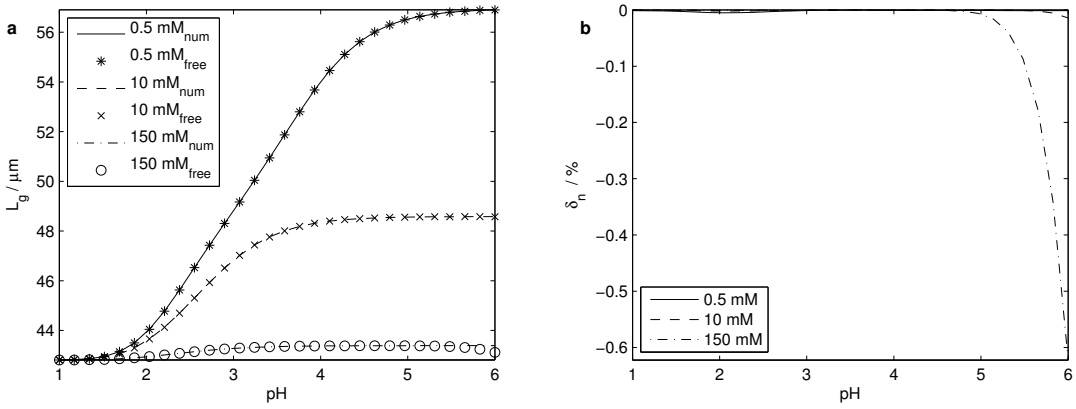

Figure 20: Comparison of unconstrained simulations and numerical calculations for homogeneous swelling when increasing pH for $AMPSA_2$. **a)** shows the axial deformation while **b)** shows the relative deviation between unconstrained swelling and numerical calculations in a).

Figure 21 shows comparison of increasing I-simulations for DMAPA_7 compared with numerical calculations for several values of pH. For pH much lower than the pK_a of 9.5, L_g^{free} is monotonously decreasing, while it is unaffected at pH-values slightly larger than the pK_a. For a pH slightly less than the pK_a, L_g^{free} increases before it decreases again, reaching a net decrease.

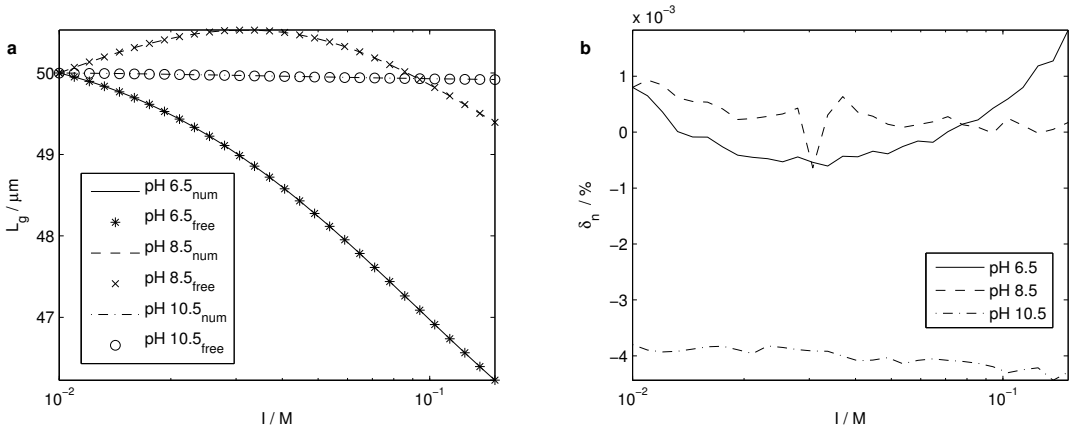

Figure 21: Comparison of unconstrained simulations and numerical calculations for homogeneous swelling when increasing I for DMAPA_7. **a)** shows the axial deformation while **b)** shows the relative deviation between unconstrained swelling and numerical calculations in a).

Figure 22 shows how the deviation between increasing pH-simulations and numerical calculations abruptly increases when the simulations approaches the range indicated in figure 12a.

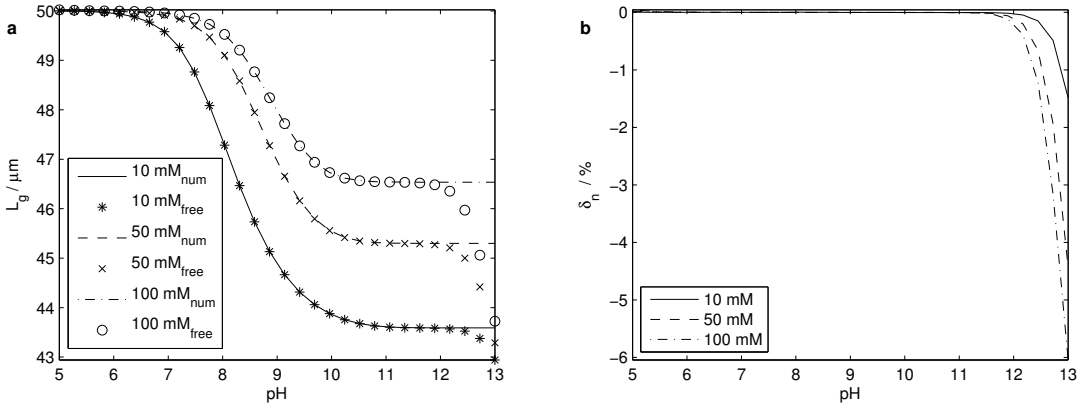

Figure 22: Comparison of unconstrained simulations and numerical calculations for homogeneous swelling when increasing pH for $DMAPA_7$. **a)** shows the axial deformation while **b)** shows the relative deviation between unconstrained swelling and numerical calculations in a).

4.2.3 Comparison of free and constrained simulations

A major part of the present study is comparing free and constrained swelling, to determine the effect of the geometrical constraints in the sensor setup. The $AMSPA_2$ gel has been used in the simulations for anionic swelling. Figures 23 and 24 show the effect of the constraints when using ionic strength and pH as the experimental parameter, respectively. Figure 23a shows that the swelling in the axial direction increases when the gel is constrained, despite the decrease in overall swelling shown in figure 23c.

The results in figure 24 also show increased swelling along the axial direction despite an overall decrease in volume when constraining the gel. This implies that the constraints of the geometry reduces the overall swelling but enhances the swelling along the unrestricted direction for the anionic gel.

For cationic swelling, the $DMAPA_7$ gel has been used in the simulations. The results in figure 25 are completely analogous to figure 23, showing that there is no principal difference between anionic and cationic swelling as a function of I. The results in figure 26 are also analogous to figure 24 with the exception that the anionic gel swells while the cationic gel shrinks with increasing pH. This implies that the constraints of the geometry reduces the overall change in volume, but enhances the swelling or shrinking along the unrestricted direction for both gels.

In figures 23 - 26, it can be observed that the deviation between the free and constrained gels increases with the degree of swelling or shrinking. The error in assuming free swelling is significant compared with the experimental

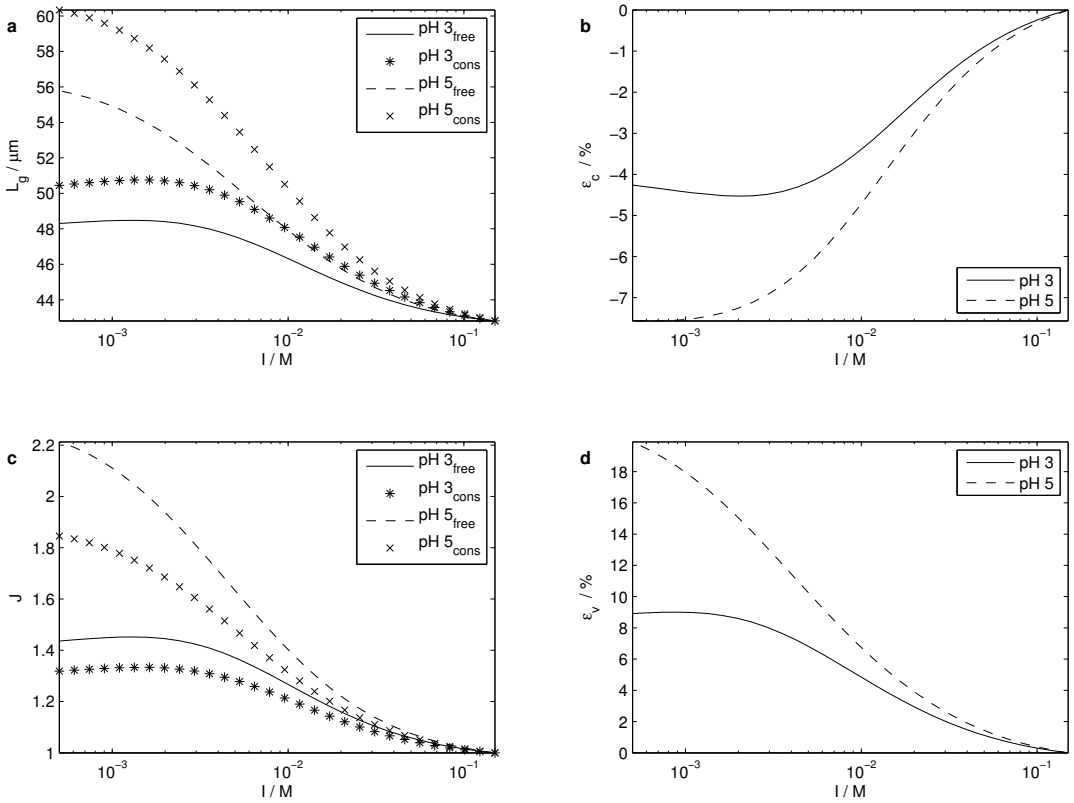

Figure 23: Comparison of free and constrained anionic swelling for $AMPSA_2$ at different pH-values. **a)** shows the swelling along the axial direction while **c)** shows the relative change in volume. **b)** and **d)** show the difference in a) and c), respectively.

accuracy and numerical precision of the simulations. The deviation in the axial length is throughout the figures opposite in sign and about half in magnitude, compared with the deviation in volume.

The electrostatic contribution to the swelling increases with the amount of fixed charges in the networks. The anionic and cationic polymer chains become charged upon proton dissociation and association, respectively. Hence, the gels behave oppositely with respect to pH as can be seen in figures 24 and 26. There it can also be confirmed that when the gels are uncharged they are insensitive to the salt concentration, and that the sensitivity increases with the charge of the gels.

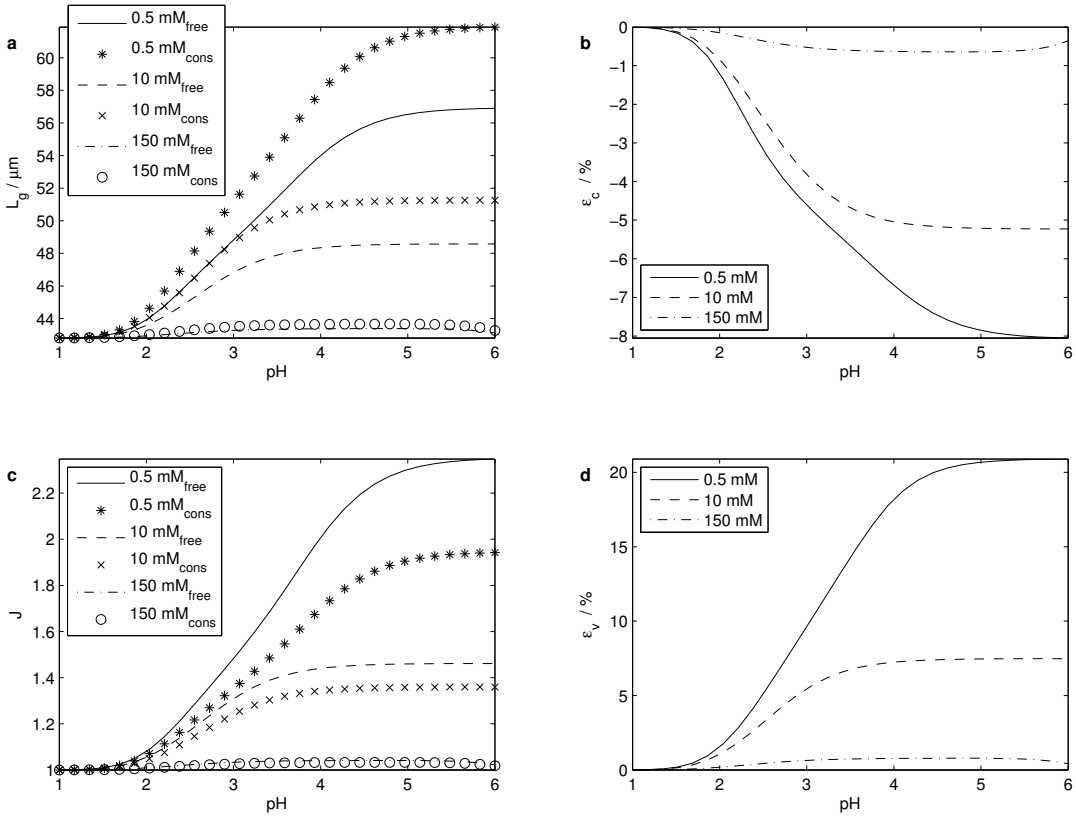

Figure 24: Comparison of free and constrained anionic swelling for $AMPSA_2$ at different ion strengths. **a)** shows the swelling along the axial direction while **c)** shows the relative change in volume. **b)** and **d)** show the difference in a) and c), respectively.

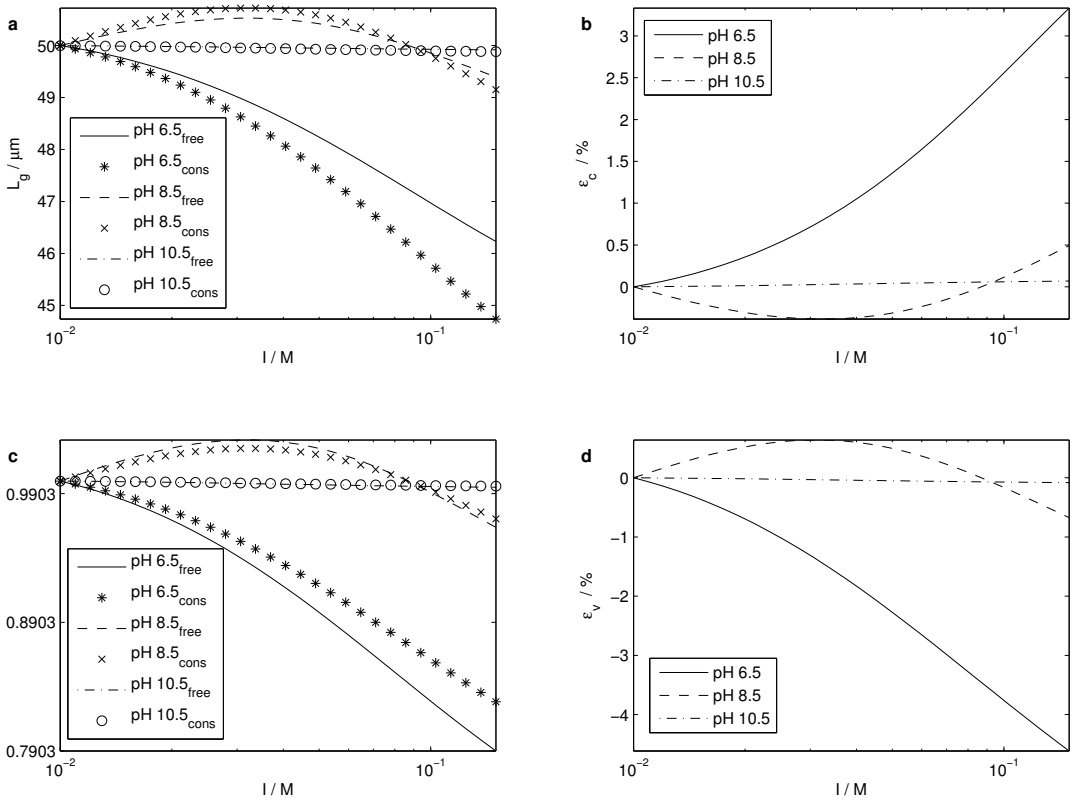

Figure 25: Comparison of free and constrained cationic swelling for $DMAPA_7$ at different pH-values. **a)** shows the swelling along the axial direction while **c)** shows the relative change in volume. **b)** and **d)** show the difference in a) and c), respectively.

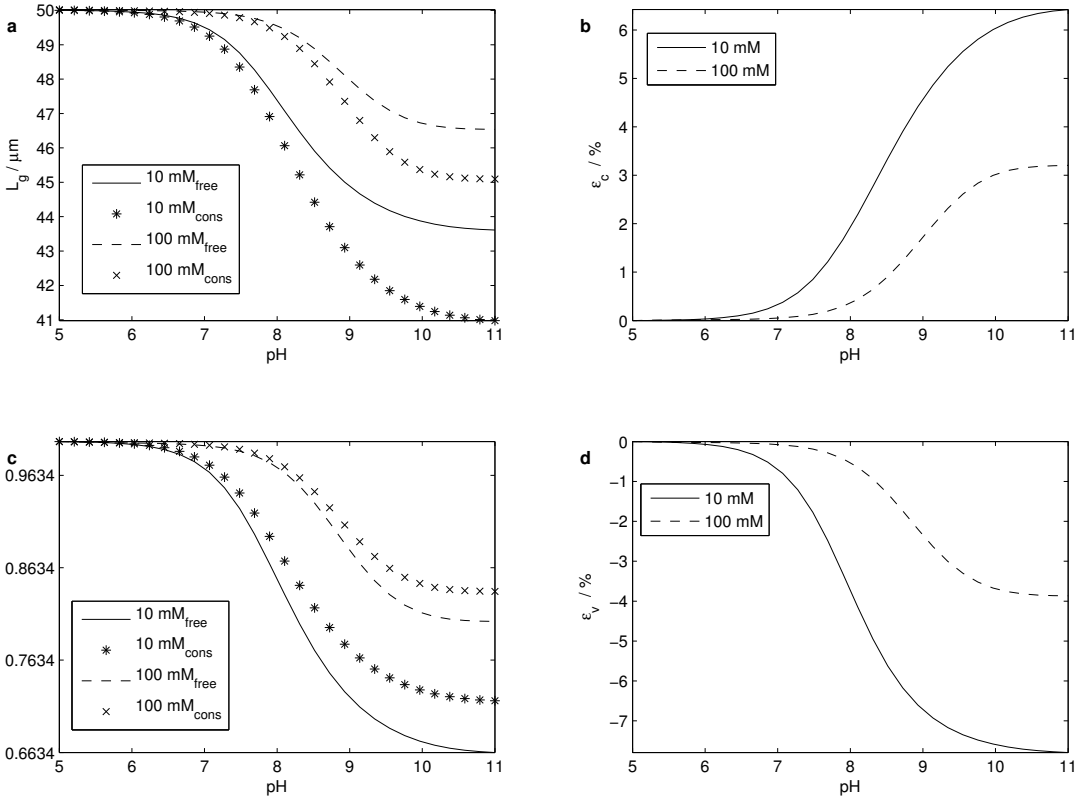

Figure 26: Comparison of free and constrained cationic swelling for $DMAPA_7$ at different ion strengths. **a)** shows the swelling along the axial direction while **c)** shows the relative change in volume. **b)** and **d)** show the difference in a) and c), respectively.

4.3 Impregnational effects

4.3.1 Shell

Figures 27 through **??** shows surface plots of constrained simulations of AMPSA$_{im}$. χ is assumed to be uniform throughout both core and shell of the gel. Figure 27a shows how the swelling capacity varies with the thickness and the network density of the shell, for a shells in the thick range. It can be seen that the equicontours starts exhibiting a linear nature in the for $vN_{shell} > vN_{core}$. Figure 27b shows the relative swelling capacity of an impregnated gel compared to an untreated one. $\epsilon_r = 50$ % for $\log_{10}(vN)$ in the range of -1.75 to -1.25.

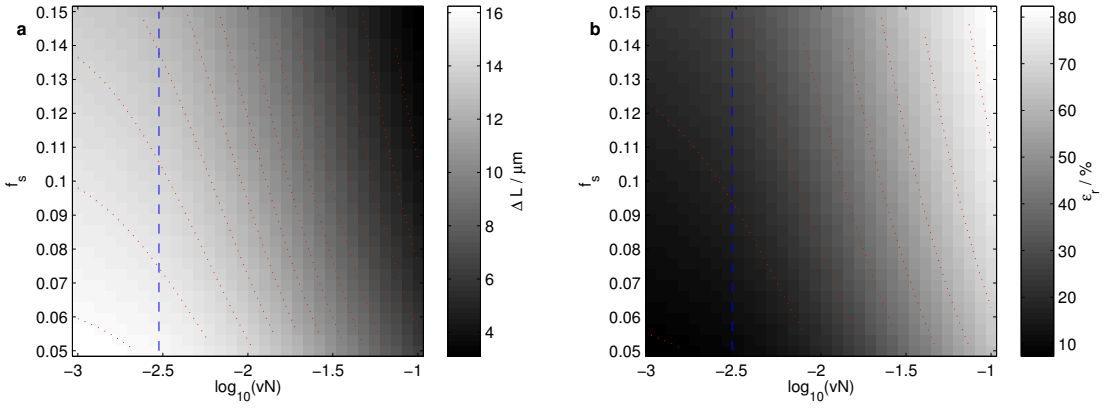

Figure 27: Surface plot of **a)** swelling capacity and **b)** relative swelling capacity as a function of vN of the shell and f_s for AMPSA$_{im}$. $I = 0.5$ mM and f_s in the range of a thick shell. The dashed line indicate the vN-value of the gels core while the dotted lines are equidistant contours with spacing of 1 µm and 10 % for a) and b), respectively.

Figure 28a shows how the swelling capacity varies with the thickness and the network density of the shell, for a shells in the very thin range. The equicontours fails to show the same linear nature in this region. $\epsilon_r = 50$ % for $\log_{10}(vN)$ in the range of -1.25 to -1.

Figure 29a plots the swelling capacity for an untreated hydrogel, together with three cases of impregnated hydrogels. The two simulated impregnated gels have vN and f_s chosen to match the reduction in swelling capacity for the untreated and experimental swelling curves, using figures 27-28 for the thick and the thin shell, respectively. It can be seen that none of the lines from impregnated gels intersect at low I, which was the requirement.

In figure 29b, the curves from a) have been normalized my their maxi-

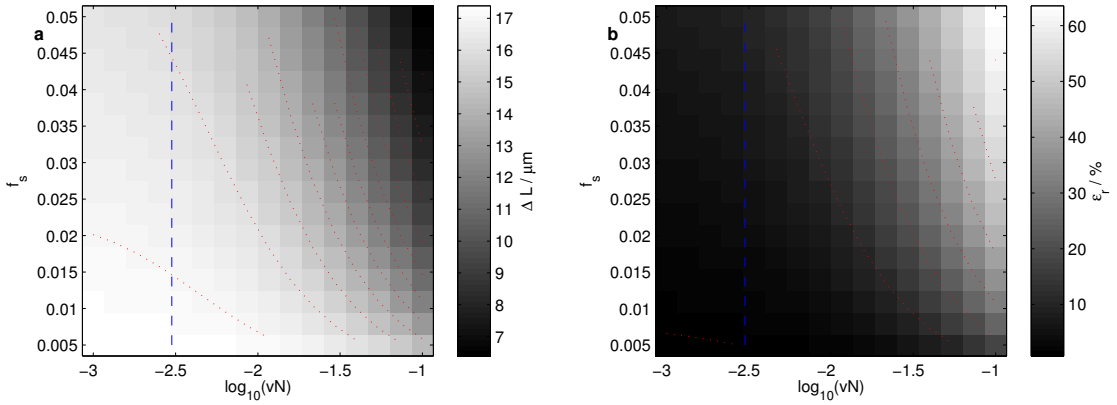

Figure 28: Same plot as figure 27, but with f_s in the range of a thin shell. The dotted lines are equidistant contours with spacing of 1 µm and 10 % for a) and b), respectively.

mum value, so the different shapes can be compared. The two impregnated simulations almost coincide, and lay above the untreated hydrogels, while the experimental curve lies below it.

Figures 30 through 32 show the $AMPSA_2$ swelling simulations from figure 29a. The stesses are given as normalized von Mises stresses, that is an non-directional stress based on all the principal stresses, and the normalization in (2.5.6). It can be seen that the stresses in the thin shell is approximately three times greater than the stresses in the shell that is about three times thicker. By comparing the grid of the optical fiber, it can be seen that figure 30 is zoomed furher out than figures 31-32, and thus is far more swollen in its end state, in agreement with figure 29a.

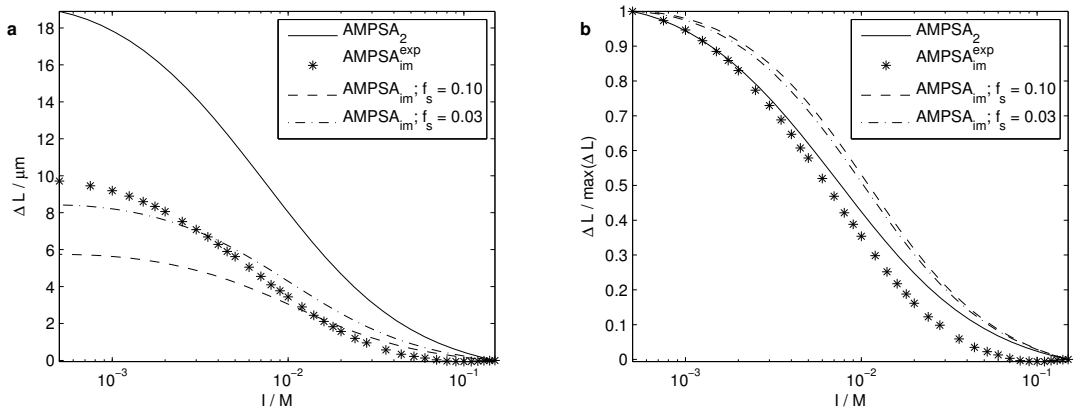

Figure 29: **a)** Swelling capacity of untreated and impregnated $AMPSA_2$ hydrogels. The impregnation simulations have a value of vN to match their value of f_s, estimated from figures 27 and 28 for the thick and the thin shell, respectively. **b)** The swelling curves from a), normalized by the highest swelling capacity in order to compare their shapes.

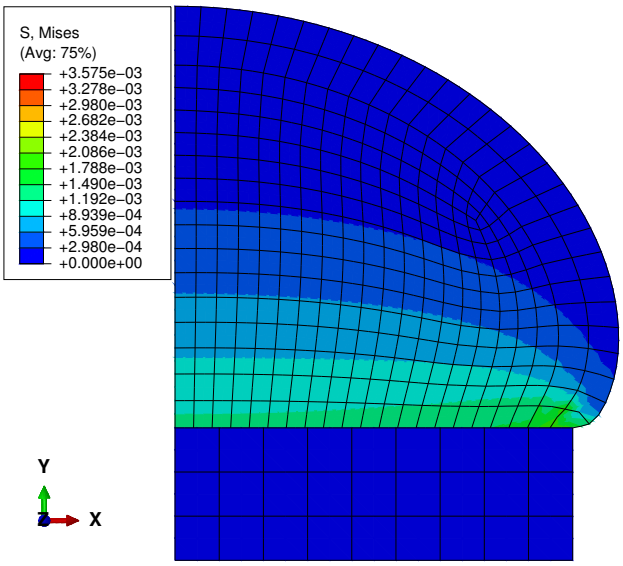

Figure 30: The untreated AMPSA hydrogel from figure 29, in its swollen state.

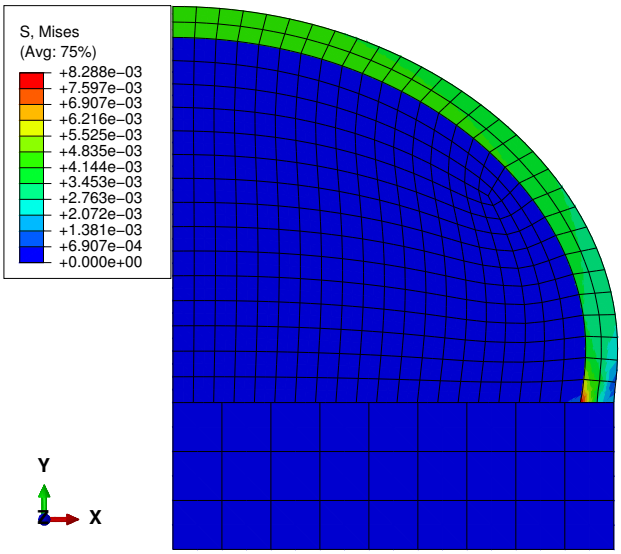

Figure 31: The impregnated AMPSA hydrogel from figure 29 with a thick shell, in its swollen state.

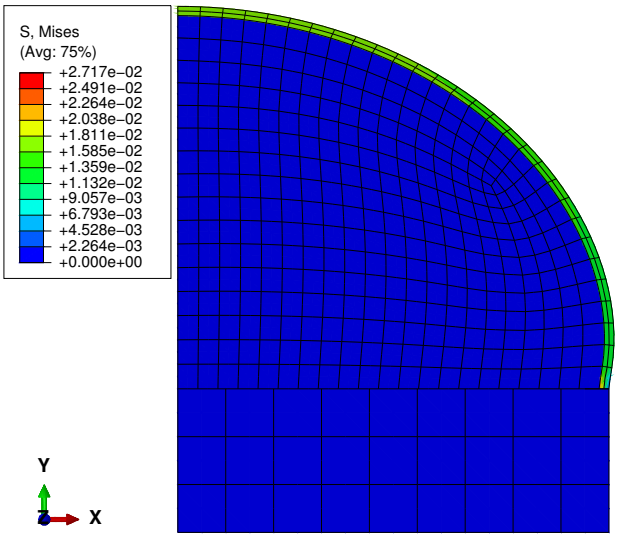

Figure 32: The impregnated AMPSA hydrogel from figure 29 with a thin shell, in its swollen state.

5 Discussion

Both the anionic and cationic material models reproduces experimental data as shown in figures 16 and 17, respectively, although the cationic material model failed to reproduce the experimental data for the DMAPA-gels in the range of $I < 100$ mM. In this range, the $DMAPA_3$-gel even swells for decreasing I, which is not handled by the current theory.

5.1 The estimated chemical parameters

The estimated parameters are given in table 6. In [5], $\chi = 0.475$ for poly-acrylamide hydrogels, while χ was found to be 0.37 and 0.41 for AMPSA and DMAPA poly-acrylamid hydrogels, respectively. The relationship between the estimated and the chemically determined value of vN, vN_{ch}, is treated in appendix A.3. It is shown that $vN_{ch} \simeq 0.06$ for both AMPSA and DMAPA. It is interesting to note that the ratio between vN and vN_{ch} is 5 % for AMPSA and 85 % for DMAPA, while the experimental data in [5] predicts a value of 23 %, as shown in figure 33 in the appendix. However, it has not been taken into consideration which crosslinker and ionizable groups being utilized in [5], and thus how valid the comparison is. The polymerization processes in [2] and [8] has neither been taken into account, so the effective values of vN_{ch} might deviate from the calculated value of 0.06.

The pK_a-value for DMAPA was estimated to be 9.5. This is considerably further away from neutral pH 7 than the midpoint of the swelling curve, with a swelling fraction of $\frac{1}{2}$, at about pH 8.6, which was assumed to be the pK_a-value in [2]. In figure 15, it can be seen that both AMPSA at pH 2 and DMAPA at pH 9.5, their respective pK_a-values, are far towards the lower plateau of the swelling curves. When only considering the effects of association and dissociation, the pK_a-value should coincide with the midpoint of the swelling curve.

However, the poroelastic contribution, U_1, will also contribute to the swelling, making the polymer chains in the network work like entropy springs. This will contribute to the total entropy balance and thusly cause the midpoint of the swelling curve to be displaced from the pK_a-value. The midpoint being skewed towards the swollen state for both the anionic and cationic networks indicate that the equilibrium point of the entropy springs is in the region of low swelling.

The swelling fraction at pH = pK_a can also be seen to be affected by the ionic strength of the external solution. The swelling fraction at the pK_a-value increases with I. This can be understood in terms of (2.4.46). When a cationic network is fully associated, negative ions will diffuse inside to

screen the positive fixed charges. This electrostatic screening increases with increasing ionic strength. When I is low the network will thus not need to absorb as much solvent to minimize Π_{ion} as if I was higher. The difference between pK_a and the fully associated gel will thus be smaller for high I than for lower I.

5.2 Comparing free and constrained swelling

Figures 20 and 22 show that the error of simulating L_g^{free} increased considerably when the range of the simulation approaches the limits sketched out in figures 11a and 12a. Even though these limits apply for the initial conditions, it will be expected that the simulations will be unable work optimally close to this range. Slow convergence has been observed in simulations approaching the end of the range before finally failing to converge when exceeding it.

The magnitude of the error when approaching the limits of the simulations is still small, and in this region the simulations approaches the point where they are unable to converge. The error is disappearingly small in the rest of the simulation region, and the correspondence between free swelling simulations and numerical calculations is thus very good.

Throughout figures 23-26, it can be seen that the effect of constraining the hydrogel to the optical fiber is to reduce the overall swelling while increasing the swelling in the axial direction. A reduction in J is to be expected while the increase in L_g has to be understood in terms the degrees of freedom in the system. Due to the constrictions along the fiber, the network will have less freedom of movement in the radial direction. It will compensate by increasing the swelling in the unconstrained, axial direction, due to the pressure from the resulting forces of the constraints.

The same effect can in the same figures be observed for shrinking, although the effect on J and L_g is opposite. The underlaying mechanisms are the same as with swelling. The deviation observed when comparing free and constrained swelling is exceeding the resolution of the sensor for a hydrogel with $L_0 = 50\mu$m, $\delta_{50} =\simeq 0.003\%$, by far for both anionic and cationic hydrogel swelling. The deviation is thus significant.

5.3 Effects of impregnation

Figure 29a shows that the contour plots in figures 27 and 28 have reduced applicability to hydrogels of different sizes, even though they show the swelling capacity and not the absolute swelling. This indicates that contour plots should be made for the specific initial geometry in order to find an accurate relation between f_s and vN.

Figure 29b indicates that the shape of the swelling curve isn't affected significantly by the constraints of a neutrally charged shell, for a given reduction in the swelling capacity. A consequence of this is that a least square estimation setup will yield a redundant solution. Furthermore, it will not be possible to reproduce the shape of AMPSA_{im}^{exp}, which data points lay below the simulation results between the endpoints of the simulation range.

Comparing figures 31 and 32, reveals that the stresses in the thin shell is about three times greater than the stresses in the approximately three times thicker shell. This is due to both figures being generated from the same reduction in the swelling capacity, with a different set of vN and f_s. To achieve this, the thickest gel would only need a third of the stress in the thin shell, spread over its larger volume. Furthermore, the stress in the shells appears to be homogeneous, with the notable exception of the interface between a shell and the optical fiber.

The shell with the highest value of vN would also experience more stress, explaining the proportionality evident in the equicontours in figure 27a. This proportionality ceases when $vN_{shell} < vN_{core}$, due to the shell no longer constricting the core elastically. The proportionality also ceases when the $f_s < 5\%$ as can be seen in figure 28a. The range of proportionality is thus $f_s > 5\%$ and $vN_{shell} > vN_{core}$ for the AMPSA_2 hydrogel impregnated with a neutral shell of thickness below 15 percent.

Due to the high resolution in determining f_s by fluorescence microscopy, and that it is possible to achieve quite thin equicontours in plots like figure 31 and 32, the value of vN can be found with a quite good resolution. However, generating high resolution contour plots for individual hydrogels is quite time consuming. Furthermore, the systematical errors of assuming an anionic gel with a sharp transition to a neutral shell has yet to be quantified.

The main advantage of this method of determining vN, is that it can be applied on a wide range of hydrogels, with Young's modulus below 10 kPa. Accurate methods of determining the properties of thin layers by measuring surface wrinkles[6] are inapplicable in the range of Young's modulus below 100 kPa.

5.4 Limitations of the subroutine

The range of the initial conditions is quite limited, as can be seen from figures 11-12, making it necessary to offset either I_0 or pH_0 from the actual value to get the simulation to converge. When doing so, one assumes that the chosen reference state is stress-free, due to the *Uhyper* subroutine requiring stress-free starting conditions[7]. While following error might be tolerable in regions where the slope of swelling curve is gentle, as can be seen in figure

10, this might not always be feasible.

The *Umat* subroutine requires the initial stresses in the simulation, together with the updated stress-profile for each step. It is thus more versatile than *Uhyper*, although its implementation is more complex. *Umat* has been shown to yield the same results as *Uhyper* for poroelastic hydrogel swelling with stress-free initial conditions[7].

6 Conclusion

The developed simulation setup for the hydrogel sensor system reproduces anionic swelling data from [8], by using the material model in [1]. It also reproduces cationic swelling data from [2], for $I > 100$ mM, by using the developed material model for cationic hydrogels. Further estimation studies must be conducted in order to validate the material model for an increased range of I.

General contour plots of the swelling capacity as a function of vN and f_s was shown to have reduced value for hydrogels differing in L_0, as can be seen in figure 29a. More information on how the contour plots of ΔL depend on L_0 needs to be obtained. Such information might be able to supplement a general contour plot in stead of generating a new plot for each gel size.

The simulation module handling the effects of gel impregnation has also been able to reproduce a reduction in the swelling capacity, as shown in [8]. Even when assuming homogeneous χ in the gel and neutral charge in the shell, there is still a redundancy in estimating vN and the thickness of the shell. The suggested method is to estimate the thickness of the shell from fluorescence microscope images and using suitable contour plots of the swelling capacity as a function of f_s and vN to get an estimate of vN.

Geometrical constrictions increases the swelling or shrinking in the axial direction, the direction being measured by the hydrogel transducer, while impregnation of the hydrogel reduces it. The change is significant compared to sensor resolution and approximations in the simulation model. The simulation setup is useful to obtain information not readily accessible by physical measurements/readouts from the hydrogel sensor, and simulation results can serve as a guide for further experiments, in particular regarding different impregnation setups.

References

[1] R. Marcombe *et al.*, Soft Matter **6**, 784 (2010).

[2] S. Tierney, D. R. Hjelme, and B. T. Stokke, Analytical Chemestry **80**, 5086 (2008).

[3] S. Tierney, B. M. Falch, D. R. Hjelme, and B. T. Stokke, Analytical Chemestry **81**, 3630 (2009).

[4] M. Queseda-Pérez, J. A. Maroto-Centeno, J. Forcada, and R. Hidalgo-Alvarez, Soft Matter **7**, 10536 (2011).

[5] U. P. Schröder and W. Oppermann, *Physical Properties of Polymeric Gels* (Wiley, 1996).

[6] J. Y. Chung, A. J. Nolte, and C. M. Stafford, Advanced Materials **23**, 349 (2011).

[7] M. K. Kang and R. Huang, Journal of Applied Mechanics **77** (2010).

[8] K. Gawel, M. Gao, and B. T. Stokke, Impregnation of weakly charged anionic microhydrogels with cationic polyelectrolytes and their swelling properties monitored by a high resolution interferometric technique. transformation from a polyelectrolyte to polyampholyte hydrogel., 2012.

[9] F. Irgens, *Continuum Mechanics* (Springer, 2008).

[10] W. Hong, X. Zhao, J. Zhou, and Z. Suo, Journal of the Mechanics and Physics of Solids **56**, 1779 (2008).

[11] L. R. G. Treloar, *The physics of rubber elasticity* (Clarendon Press, 1975).

[12] P. J. Flory, *Principles of polymer chemistry* (Cornell University Press, 1953).

[13] W. Hong, X. Zhao, and Z. Suo, Journal of the Mechanics and Physics of Solids **58**, 558 (2010).

A Further mathematical relations

A.1 Solution of a cubic equation

Solution of the cubic equation

$$ax^3 + bx^2 + cx + d = 0, \tag{A.1.1}$$

takes the following form:

$$x = \sqrt[3]{q + \sqrt{q^2 + p^3}} + \sqrt[3]{q - \sqrt{q^2 + p^3}} - \frac{b}{3a} \tag{A.1.2}$$

where

$$p = \frac{c}{3a} - \left(\frac{b}{3a}\right)^2 \tag{A.1.3}$$

$$q = \frac{1}{2}\left(\frac{bc}{3a^2} - \frac{d}{a}\right) - \left(\frac{b}{3a}\right)^3. \tag{A.1.4}$$

This can be verified by inserting (A.1.2-A.1.4) back into the left side of (A.1.1), yielding zero.

A.2 Swelling for different geometries

The aim of this section is to derive the expressions for the gel length L_g depending on the geometry. For the sensors being modeled, a hemiellipsoidal geometry is used, while for the case of homogeneous swelling, a spherical geometry is applied. This yields different relations between the gel length and the swelling.

$$J_0 = \frac{V_0}{V_d} \tag{A.2.1}$$

$$J_{tot} = \frac{V}{V_d}. \tag{A.2.2}$$

Inserting (A.2.1) into (A.2.2) yields

$$\frac{V}{V_0} = \frac{J_{tot}}{J_0}. \tag{A.2.3}$$

Hemiellipsoid

Volume of hemiellipsoid with two of the half-axis equal to r_f and the last one equal to L_g:

$$V = \frac{1}{2}\frac{4}{3}\pi r_f^2 L_g \tag{A.2.4}$$

and thus

$$V_0 = \frac{1}{2}\frac{4}{3}\pi r_f^2 L_0 \tag{A.2.5}$$

where L_0 is the gel length at a stress-free state. (A.2.3) can be written as:

$$L_g = \frac{J_{tot}}{J_0} L_0 = J L_0. \tag{A.2.6}$$

Sphere

Volume of sphere with radius equal to L_g:

$$V = \frac{4}{3}\pi L_g^3 \tag{A.2.7}$$

and thus

$$V_0 = \frac{4}{3}\pi L_0^3. \tag{A.2.8}$$

(A.2.3) can be written as:

$$L_g = \frac{\lambda_{tot}}{\lambda_0} L_0 = \lambda L_0. \tag{A.2.9}$$

A.3 Chemically estimated crosslink density

The known chemical composition used in polymerizing the hydrogel can be used in a mathematical estimate of vN. The chemical parameters that are relevant for this section are listed in table 23. The molfraction of crosslinkers is given by

$$f_X = \frac{N_X}{N_M}, \tag{A.3.1}$$

while the number of monomers per crosslink can be estimated by

Table 23: Parameter definitions for the section.

k	g/cm^3	Monomer weight fraction
ρ	g/cm^3	Monomer density
f_X	1	Molfraction crosslinker
F	1	Crosslink functionality
N_M	#/m^3	Monomers per volume
N_X	#/m^3	Crosslinkers per volume
vN_{ch}	1	Crosslinks per monomer

$$\frac{1}{vN_{ch}} \simeq \frac{N_M}{F \cdot N_X} = \frac{1}{f_X \cdot F}. \tag{A.3.2}$$

Eq. (A.3.2) can be rearranged to express vN_{ch}:

$$vN_{ch} \simeq f_X \cdot F. \tag{A.3.3}$$

Lastly, λ_0 can also be calculated from the weight fraction of polymers:

$$\lambda_0 = \sqrt[3]{\frac{1}{\phi_N}} = \sqrt[3]{\frac{\rho}{k}}. \tag{A.3.4}$$

Table 24 shows the provided and estimated parameters for the AMPSA and DMAPA hydrogels. The values of vN_{ch} is then compared with the values of vN in table 6, and the ratios between vN and vN_{ch} is then compared with experimental data from [5], in figure 33.

Table 24: See table 23 for units.

Gel	k	ρ	f_X	F	vN_{ch}	λ_0
AMPSA	0.10	1.13	0.03	2	0.06	2.244
DMAPA	0.15	1.13	0.03	2	0.06	1.960

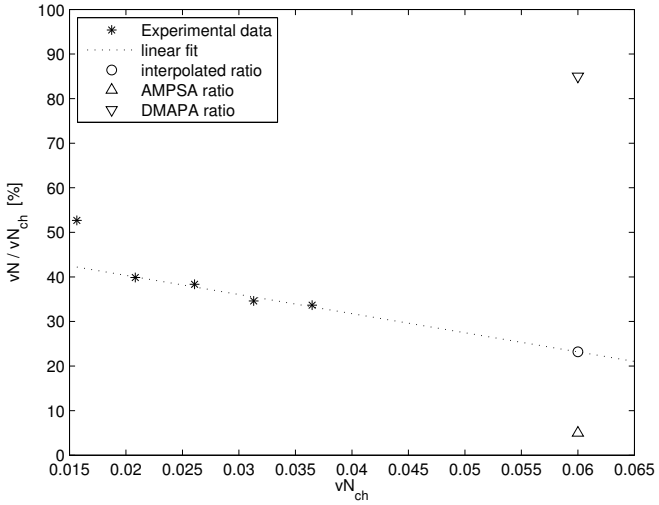

Figure 33: Ratio between effective and chemically determined crosslink density. The experimental data are reproduced from table 1 in [5]. The estimated values of vN are from table 6.

B Setting up a model in MATLAB

B.1 Initial preparations

The simulation framework requires two file directories, denoted **dirPath** and **wsPath** for *MATLAB* and for *ABAQUS*, respectively, and a workspace directory denoted **myPath** for the abaqus job files and the generated input and output files. The contents of **wsPath** should be a folder called *bin* with the following contents:

- createOutput.py
- Sensor.py
- Uhyper_multi.f
- Template.cae

Template.cae is a default *ABAQUS*-simulation that can be copied into **myPath** and renamed for every new .cae file needed. It can be many **myPath** directories for different kinds of simulations, but all of them have to contain a *in* and *out* folder, together with a .cae file that will be the target of the variable simName in *MATLAB*. A default **myPath** folder called *Default*

should be created within **wsPath**, containing Default.cae. The contents of **dirPath** should be a folder *out* for generated .mat files, and a folder *bin* containing:

- AbaRunner.py
- getGel.m
- getSimInfo.m
- updateGel.m
- getData.m
- getFreeData.m
- makeInputFile.m
- get_JtotFree.m
- get_sigma11.m
- get_vcH.m

B.2 Functions

The help files of the essential *MATLAB* functions in the simulation framework:

getGel.m

```
% function gel = getGel(gelName)
%
% Returns a requested gel struct
%
% INPUT
% gelName - string with gel name
% OUTPUT
% gel - gel struct matching gelName, or list of gels of no match was found
```

updateGel.m

```
% function gel = updateGel(g)
%
% Updates the geom and chemProps arrays in the input gel struct
%
% INPUT
% g - gel struct to be updated
% OUTPUT
% gel - updated gel struct
```

getSimInfo.m

```
% function simInfo = getSimInfo(endVal, nSteps, N, myPath, simName, jobDescr)
%
% Retrieves a simulation struct. wsPath should be edited in this function
% or be set afterwards by: simInfo.wsPath = '/path/to/workspace/'.
%
% INPUT
% endVal - End of simulation range (I or pH)
% nSteps - number of simulation steps
% N - Model/job number
% myPath - path to simulation workspace
% simName - simulation name
% jobDescr - job description
%
% OUTPUT
% simInfo - simulation struct; describin the simulation
```

getData.m

```
% function [axis,Lgel,J,lam0] = getData(gel,simInfo,scriptName)
%
% Runs makeInputFile and a python script to link with ABAQUS.
% Retrieves simulation results.
%
% INPUT
% gel - gel struct
% simInfo - simulation struct
% scriptName - name of the python script to link with ABAQUS
% OUTPUT
% axis - axis of the simulation. Either I or pH, depending on simInfo
% Lgel - Gel length
% J - relative volume change
% lam0 - length change at reference state
```

getFreeData.m

```
% function [axis,Lg,J,lam0] = getData(gel,simInfo)
%
% Retrieves numerical calculations for stress-free swelling.
%
% INPUT
% gel - gel struct
% simInfo - simulation struct
% OUTPUT
% axis - axis of the simulation. Either I or pH, depending on simInfo
% Lgel - Gel length
% J - relative volume change. Practically equal to J0
% lam0 - length change at reference state
```

makeInputFile.m

```
%function [statusFlag, lam0] = makeInputFile(gel, simInfo)
%
% Generates the input file to be read from the python script linking the
% simulation with ABAQUS using the information in gel and simInfo
%
% INPUT
% gel - gel struct containing the defining gel parameters
% simInfo - simulation struct containg simulation info
% OUTPUT
% statusFlag - 1 if successful, 0 if no file was created
% lam0 - array containg lam0 for the anionic and cationic material
```

get_JtotFree.m

```
% function [JtotFree, sigma11, vcH, sigma11_0] = get_JtotFree(PROPS,J0J,salt,pH,interpFlag)
%
% Calculating a Jtot matrix from PROPS and the intervals.
% Passes on input parameters to get_sigma11(PROPS,J0J,salt,pH).
%
% INPUT
% PROPS - array with the characteristic gel parameters. Use gel.chemProps
% J0J - Search/calculation interval of J0J. J0J = 1:.01:500 is suggested
% salt - Result interval for ionic strength
% pH - Result interval for pH
% interpFlag - 1: allowing linterploation, 0: closest neigbour fit
%
% OUTPUT
% JtotFree - Jtot for free swelling
% sigma11
% vcH - molecular volume times proton concentration
% sigma11_0
```

get_sigma11.m

```
% function [sigma11, vcH] = get_sigma11(PROPS,J0J,salt,pH)
%
% Calculating a sigma11 matrix from PROPS and the intervals.
% Passes on input parameters to get_vcH(PROPS,J0J,salt,pH).
%
% INPUT
% PROPS - array with the characteristic gel parameters. Use gel.chemProps
% J0J - Search/calculation interval of J0J. J0J = 1:.01:500 is suggested
% salt - Result interval for ionic strength
% pH - Result interval for pH
%
% OUTPUT
% sigma11
% vcH - molecular volume times proton concentration
```

get_vcH.m

```
% function vcH = get_vcH(PROPS,salt,pH, J0J)
%
% Calculating a vcH matrix from PROPS and the intervals.
% Passes on input parameters to get_vcH(PROPS,J0J,salt,pH).
%
% INPUT
% PROPS - array with the characteristic gel parameters. Use gel.chemProps
% J0J - Search/calculation interval of J0J. J0J = 1:.01:500 is suggested
% salt - Result interval for ionic strength
% pH - Result interval for pH
%
% OUTPUT
% vcH - molecular volume times proton concentration
```